Experimental Investigations of Microchannel Cooling within a Nozzle Guide Vane Trailing Edge Configuration

Undergraduate Honors Thesis

Submitted in Partial Fulfillment of Requirements

For Graduation with Distinction in Mechanical Engineering

The Ohio State University

Department of Mechanical & Aerospace Engineering

April 2017

Author

James Walsh

Defense Committee

Dr. Jeffrey Bons, Thesis Advisor

Dr. James Gregory

Abstract

Improving component cooling to sustain higher gas turbine inlet temperatures is a widely-studied subject to improve engine efficiency. From advances in additive manufacturing technology, the use of microchannel cooling is possible within turbine components and appears advantageous due to significant heat transfer benefit within a small packaging and the ability to provide targeted cooling [1]. Although microchannel usage at relevant engine conditions has been characterized in prior research [16,18], application into a trailing edge geometry and direct comparison to current trailing edge cooling technologies has yet to be explored. The purpose of this study is to characterize the heat transfer performance of near surface microchannel cooling within a trailing edge configuration for direct comparison to current cooling technologies. The current cooling technologies tested were ribbed turbulators and a pin fin array. Utilizing bulk flow analysis and the Thermal Inertia HTC technique, effective surface heat transfer rates were determined and compared for the three cooling configurations within the same trailing edge geometry. Cooling performance parameters evaluated within testing include Nusselt number, and pressure drop. Near surface microchannel cooling shows potential for improvement to surface heat transfer at higher Reynolds numbers. Although there is a large pressure drop within the microchannel, utilizing a denser array of microchannels would reduce the pressure drop across the test article and could produce an overall improvement to cooling efficiency. This increase in cooling efficiency would require less mass flow to be utilized for component cooling, increasing the mass flow for power generation. Near surface microchannel cooling proves promising to produce efficiency increases in future gas turbine engines.

Acknowledgements

I would like to thank my family for supporting me throughout this research in every way possible. To my Mother and Father, I could not have accomplished all that I have in my life without your guidance and wisdom. To my brother Kevin, thank you for constantly pushing me to achieve more and think more deeply. To my sister Erin, thank you for always knowing exactly what to do to bring a bright spot to my day or distract me when it is most needed. Lauren, thank you for your constant understanding and support throughout this research. You are my rock, and the person that I can count on most to be there for me, no matter how difficult a situation that I am presented with.

My deepest gratitude goes to Dr. Jeffrey Bons for his wisdom and for providing me the opportunity to pursue this research. It has been an invaluable opportunity to explore gas turbine heat transfer and take my first steps into research. I would also like to thank Dr. James Gregory and Dr. Ali Ameri for their guidance throughout my work. To my fellow members of the Turbine Aerothermodynamics Laboratory, thank you for your continuous support and guidance throughout my research. This work has been sponsored with funding from the U.S. Department of Energy (NETL) under the UTSR Program. Computational resources were provided by the Ohio Supercomputer Center. I would like to thank both organizations for their contributions to this work.

Table of Contents

List of Figures

List of Tables

Nomenclature

A	Surface Area
A_{cs}	Cross-Sectional Area
A_{max}	Pin cross-sectional area
$A_{cs,feature}$	Cross-sectional area of the combined channels
c_p	Specific heat of the convective fluid
D	Pin Diameter
D_h	Hydraulic Diameter
e	Height of a Rib
f_{Dh}	Duct friction Factor
h	Heat Transfer Coefficient
$\bar{h}$	Average Heat Transfer Coefficient
h_n	Heat transfer coefficient at the nth iteration of the heat transfer model
h_{n+1}	Heat transfer coefficient at iteration n+1 of the heat transfer model
H	Height
k	Thermal Conductivity of a fluid
L	Length
L_c	Characteristic Length
$L_{channel}$	Channel length
$\dot{m}$	Mass flow rate
N	Number of Items (multiplier)
Nu	Local Nusselt Number
$\overline{Nu}$	Average Nusselt Number
p	Pressure
p	Rib-to-rib pitch
Δp	Pressure drop
P	Perimeter
Pr	Prandtl Number
q	Heat Transfer Rate
Re_D	Reynold's Number for Pin
Re_{Dh}	Reynolds Number for Ducts
S	Spanwise spacing of pins

t	Time
T_s	Surface Temperature
$T_{initial}$	Temperature of test article at isothermal condition prior to test
$\bar{T}_{inlet}$	Average inlet temperature
$T_{coolant}$	Convective fluid temperature
$\bar{T}_{outlet}$	Average outlet temperature
u	Streamwise Flow Velocity
u_m	Mean streamwise flow velocity
w	Width of a Rib
x	Distance normal to the measured surface within the heat transfer model
X	Streamwise spacing of pins
y	Spanwise distance along the measured surface within the heat transfer model
z	Streamwise distance along the measured surface within the heat transfer model
α	Rib angle-of-attack
ρ	Fluid density

Chapter 1: Introduction

1.1 Background

Gas turbine engines have been successfully used for land-based power generation and aircraft propulsion for decades. Within these applications, gas turbines hold the distinct advantages of having a large thrust-to-weight ratio and being a reliable source of power generation. As shown in Figure (1) below, gas turbines consist of four primary regions: the inlet, the compressor, the combustor, and the turbine.

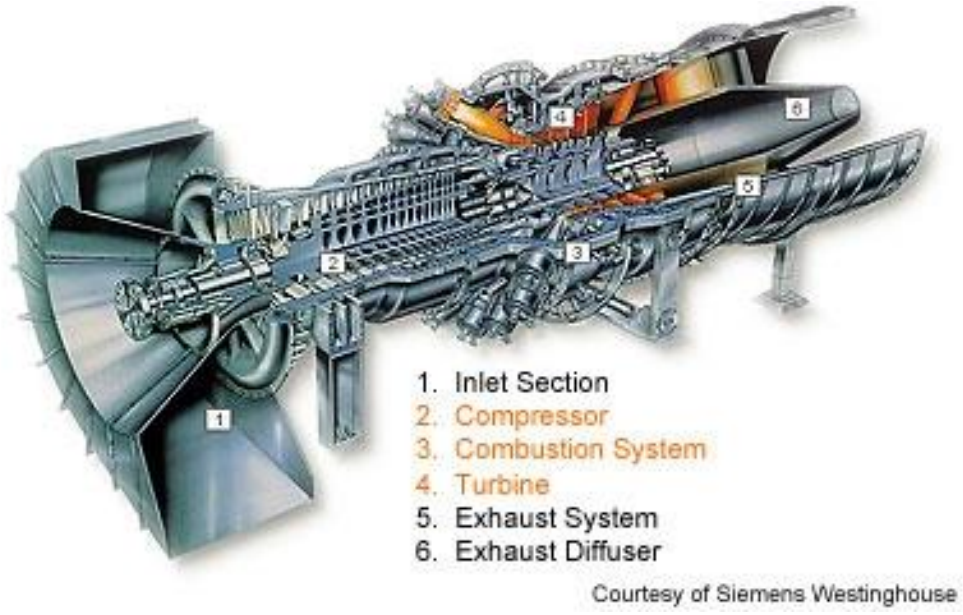

Figure 1: Siemens Westinghouse Gas Power Turbine [2]

Gas power turbines operate on a standard Brayton Cycle in which three thermodynamic processes occur: compression, combustion, and expansion. Within operation, the working fluid enters the compressor stages via the inlet and undergoes compression through each compressor stage. This compression increases the pressure and temperature of the working fluid as it enters the combustor. From the addition of fuel, air entering the combustor combusts and forms a gaseous high energy product which is expelled into the turbine. Within the turbine, work is extracted from expanding air by the turbine stages via turbine blades mounted to disks on a rotating shaft or blisks mounted to a rotating shaft. This work is utilized to provide power output and to drive the compressor stage of the engine for further power generation. Within more complex gas turbines, multiple turbine stages can be utilized to extract higher amounts of work and drive additional

compressor stages via spools. Within many land-based gas power turbines, exhaust gases are routed to accessory equipment for the removal of excess energy from the hot expelled gas, or for use in regeneration. The primary differences between land-based gas power turbines and gas turbines utilized for aircraft propulsion, from an operation perspective, are based in the use of energy extracted from the turbine stage. Land-based turbines utilize energy extracted from the turbine to create shaft driven power output and operate the compressor stage of the gas turbine. Air-breathing jet engines utilize work not extracted from the turbine stage to generate thrust via nozzle ejection aft of the turbine stage while only a small portion of energy is used to drive the compressor stages.

Efficiency within a gas turbine engine is primarily dictated by the compressor pressure ratio within the engine. If pressure is increased in the compressor, working fluid entering the turbine stages will increase in both temperature and pressure, allowing for more work to be extracted across the turbine stages from fluid expansion. Increasing temperature at the turbine inlet causes great concern for component durability as temperatures currently exceed the thermal capabilities of the materials used to create turbine components. With the growing need for more efficient gas turbines within power generation applications, advanced cooling technologies and material development are necessary to achieve current component durability targets at higher temperatures within primary stage turbine components.

Within current gas turbine engines, three technologies allow turbomachinery components to operate in the harsh and high temperature gases expelled from the combustor into the turbine: improved material thermal capabilities, thermal barrier coatings, and advanced internal and external cooling technologies. Figure (2) offers insight into how these advancements have allowed significant increases in gas temperature at the turbine inlet over time.

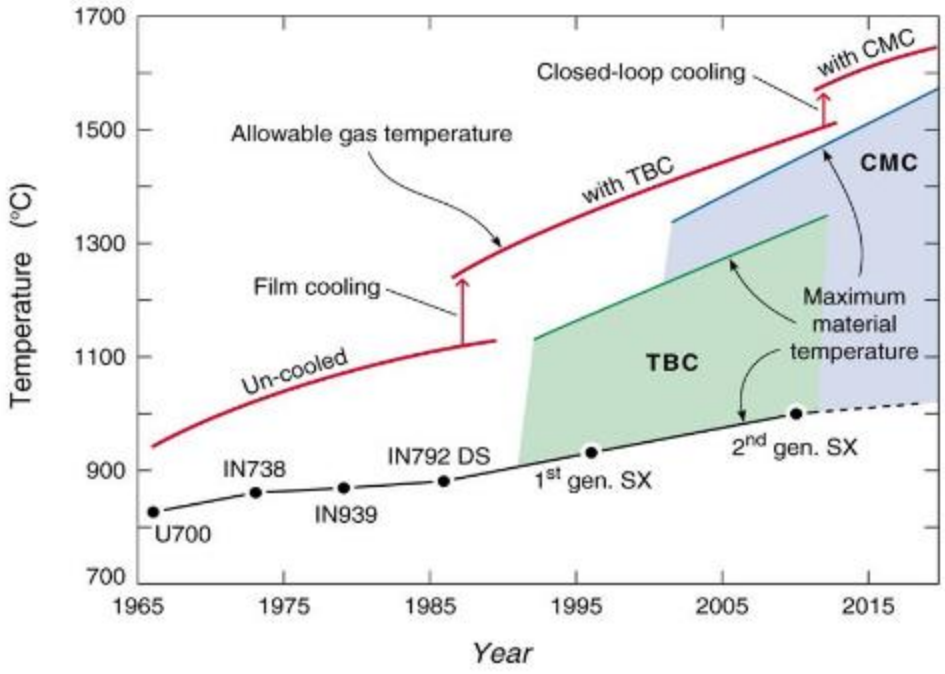

Figure 2: The evolution of allowable gas temperature at the turbine inlet with advances in component material properties, cooling technologies, and protective strategies [3].

In the 1960s and into the late 1980s, operating temperatures within the turbine were driven by thermal capability of materials used within the turbine components. With the development of nickel-based super alloys and ceramic matrix composites (CMCs), base material thermal capability has significantly increased, allowing for much higher operating efficiency of the engine. Thermal barrier coatings are material systems applied to turbine components that act as insulators of cooled components and allow for the application of sustained heat loads by working fluid as gases exit the combustor. (I'm sure you realize this, but TBCs only help if you internally cool the parts.) Application of these coatings allows for a 200°C – 250°C increase in permissible operating temperature within turbine components and provides a significant increase in component life, as shown in Figure (2). Cooling technologies present within turbine components can be broken into internal cooling technologies and external cooling technologies as shown in Figure (3) & (4).

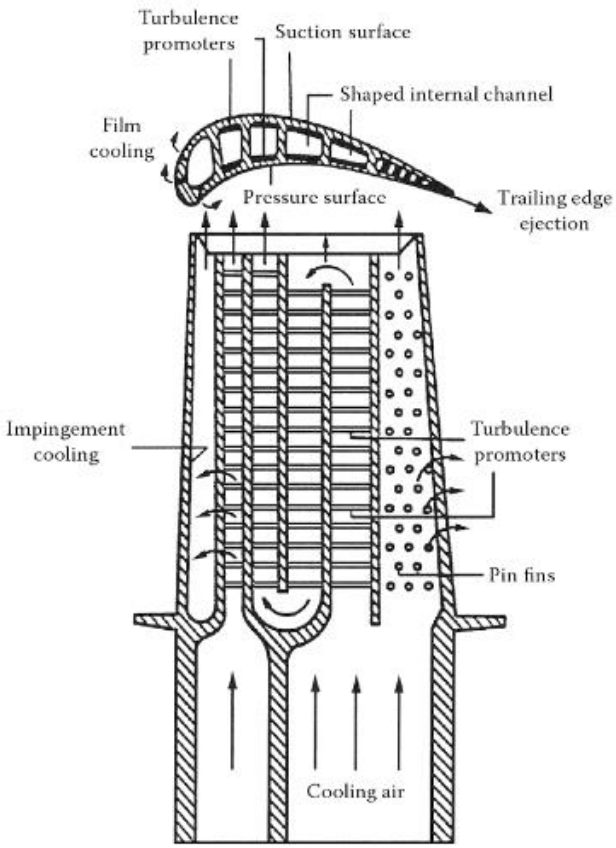

Figure 3: Cooling technologies present within modern gas turbine high pressure turbine blade [4]

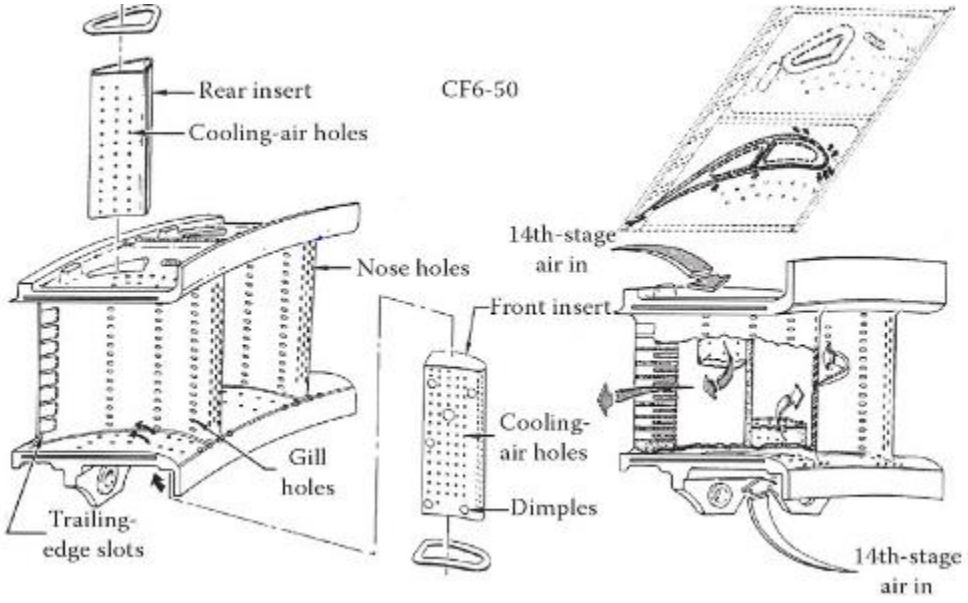

Figure 4: Cooling Technologies present within GE CF6-50 Stage 1 High Pressure Turbine Nozzle Guide Vanes [4]

The purpose of external cooling is to provide a protective layer of cool air along the surface of the vane to insulate the component surface from exposure to the high temperature working fluid. This is primarily accomplished through the implementation of film cooling holes along the surface of the airfoil upstream of critical hot spots on the blade or vane to allow coolant to cover this region with compressor bleed air. Internal cooling technologies vary by region of the blade or vane to accommodate for specific cooling needs of the region. Impingement cooling is often utilized on the leading edge internal surface to combat the large heat load applied to the stagnation region of the leading edge outer surface. Ribbed turbulators are commonly found within the internal serpentine cooling passages of modern vanes to augment heat transfer by inducing turbulence with minimal pressure losses throughout the passage. Pin fins are a staple in trailing edge cooling as they provide both a method of inducing turbulence (and thus heat transfer) while helping maintain the structural integrity of the slim trailing edge region. Despite the success of modern cooling technologies, increasing efficiency needs within power generation have spawned the need to devise novel cooling strategies to increase thermal capability of turbine components. This holds particular stead in the trailing edge region as survivability of this region is a primary concern within the cooling of first stage turbine vanes. One novel strategy that has gained traction within this region is the use of microchannel cooling. The current study is posed to determine the effectiveness of microchannel cooling when compared to pin fin and ribbed turbulator cooling configurations.

1.2 Motivation and Objectives

The origins of microchannel cooling are in CPU and electronics cooling [1]. The benefit seen by microchannels within these applications is large heat transfer coefficients with minimal space consumption. This is due to Newton's Law of Cooling, which dictates that, for a fixed temperature difference, heat flux is dictated by the quantity hA where h is the internal channel heat transfer coefficient and A is the surface area over which heat transfer occurs. Microchannels have a very high surface area per unit volume, so densely packaging microchannels within an array poses an innovative solution to generating large amounts of heat transfer within a body.

Although previously unavailable for use in aerospace and gas turbine applications, advances in additive manufacturing have opened the possibility to implement these compact

cooling structures into gas turbine components. Additive manufacturing is the process of creating a three-dimensional object utilizing computer controlled layering of material upon itself. This technology creates an interesting design problem, as it vastly increases the threshold of possible component geometries that can be manufactured. In addition, the capability of additive manufacturing technologies to produce rapid prototypes allows for development and testing of numerous designs at a reduced cost when compared to industry standard design cycles. Rather than being constrained by available manufacturing processes and prolonged prototype development cycles, design for additive manufacturing within practical application is primarily limited by the size of the machine build envelope, constraints due to anisotropic material properties, and the need to design support structures for overhanging regions with respect to the build direction. Table 1 below provides a list of just a few of the additive manufacturing processes available for commercial use today.

Table 1: Additive Manufacturing Processes

	Stereolithography	**Fused Deposition Modeling**	**Direct Metal Laser Sintering**
Materials	Plastics (HDPE, APB)	Thermoplastics	Metals
Process Overview	Layer Plastic & Harden with Laser	Heat Bottom Surface, Extrude Plastic Upward, Let Material Harden and Extrude More	Apply Powder Layer, Use to weld materials on Micron Level, Apply Additional Powder Layer
Use in Turbomachinery Applications	No	No	Yes

Direct Metal Laser Sintering (DMLS) is of particular interest to the gas turbine industry, as a number of production grade additive materials are becoming more widely available. These materials include nickel-based super alloys and materials with significant thermal capabilities. Additive manufacturing has also proven to be capable of producing parts that can withstand the harsh environment of the turbine, as shown by Siemens Power and Gas Division's recent testing of additively manufactured turbine blades. The promising benefits of microchannel cooling and capability to manufacture microchannels within a gas turbine vane or blade have led researchers

to begin exploring the capabilities of additively manufactured microchannels for future use in gas turbine application.

The goal of this research is to comparatively analyze the heat transfer performance of microchannel cooling when compared to state-of-the-art cooling configurations. The potential benefits of microchannels for near-surface cooling of the trailing edge region will be explored within a nozzle guide vane. Although available studies have provided details regarding heat transfer performance of microchannels within gas turbine components, the use of this cooling configuration within a trailing edge geometry has yet to be explored for heat transfer performance in the public domain.

Experimental data was taken for each of the cooling configurations discussed. Heat transfer performance was characterized via bulk flow analysis and the Thermal Inertia Heat Transfer Coefficient technique for use in comparative analysis of each cooling configuration. Chapter 2 describes prior research conducted on ribbed turbulators, pin fin arrays, and microchannel cooling. Chapter 3 provides a description of the experimental facility, test article design, and testing protocol. Chapter 4 discusses the results of the bulk flow analysis, 3D inverse transient model analysis, and provides an evaluation of mass flow performance based on pressure drop across each test article. Finally, Chapter 5 provides conclusions derived from the present work and recommendations for future work.

Chapter 2: Literature Review

2.1 Cooling Requirements for Trailing Edge

As shown in Figure (3) below, the hottest portion of a cooled nozzle guide vane is located in the trailing edge region. The heat transferred to first stage vanes is primarily influenced by combustor outlet temperature profile, high free-stream turbulence, and hot streaks [4], creating a particularly harsh environment for the component. This region is particularly difficult to cool as the airfoil geometry necessary to satisfy aerodynamic requirements of the vane lead to the trailing edge geometry having minimal thickness. The slim profile in this region creates a unique problem to the designer. The minimal thermal mass of this geometry causes durability issues as high temperatures in this region cause degradation of the part at a faster rate than the vane body. However, concerns for structural integrity also inhibit many proven cooling configurations from providing coolant near the surface of the trailing edge region.

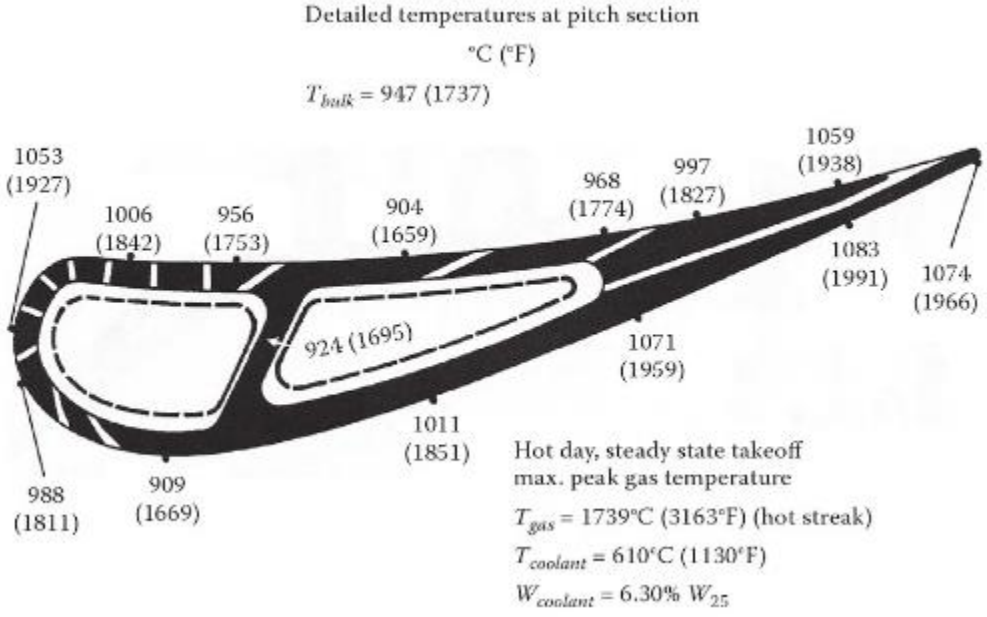

Figure 5: E3 stage-1 HPT vane pitch section detailed temperature distribution. (From Haila, E.E. et al., Energy efficient engine, General Electric Company, Fairfield, CT (prepared for NASA CR-167955), 1982. With Permission) [4]

Therefore, an ideal cooling technology in this region would provide near-surface cooling while maintaining the structural integrity of the vane trailing edge. Current cooling technologies utilized within this region include Pin-Fin Arrays and Pedestals. Although useful for providing

heat transfer to the trailing edge surface, Pedestals were not evaluated in the present study. Ribbed Turbulators were included in the present study as a replacement since they are a prominent cooling technology within the serpentine cooling channels forward of the trailing edge (see Fig. 3).

2.2 Conventional Trailing Edge Cooling Configurations

2.2.1 Ribbed Turbulators

As discussed within [4], heat transfer is augmented by ribbed turbulators through several mechanisms. The primary method of heat transfer that occurs within rib turbulator arrangements is induced by reattachment of the boundary layer on the heat transfer surface. Separation of the boundary layer also increases heat transfer via turbulent mixing of the near surface fluid with bulk flow of the internal channel. Pressure drop induced near the rib surface has negligible effect on the overall bulk flow within the internal cooling channel of a Nozzle Guide Vane when compared to the net benefit received from augmented heat transfer performance. The negligible pressure effect of this configuration makes them an adequate solution for heat transfer augmentation within a Nozzle Guide Vane. Figure (6) below displays parameters utilized within numerous studies to evaluate heat transfer augmentation from ribbed turbulator configurations.

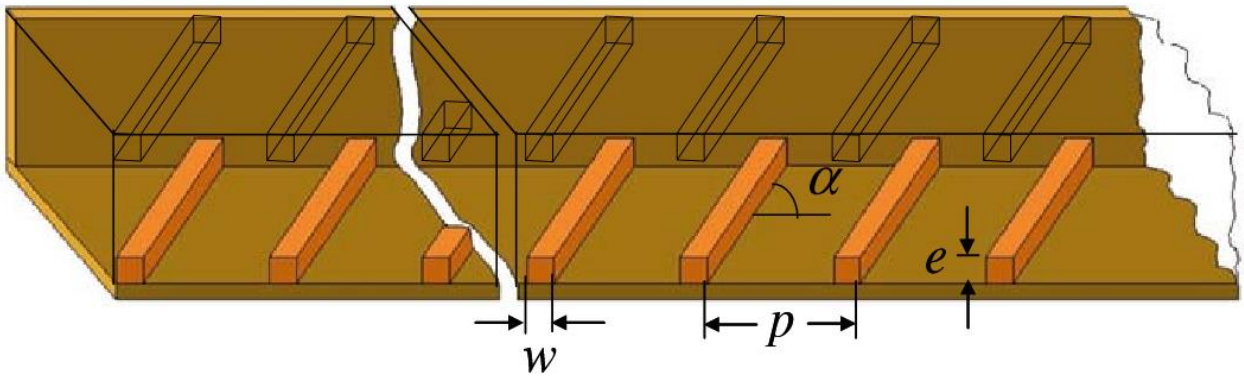

Figure 6: Design Parameters for a Ribbed Turbulator configuration [6]

Within Figure (6), *e* is the height of a rib, *w* is the width of a rib, *p* is the rib-to-rib pitch (otherwise known as the rib spacing), and α is the rib angle of attack. Within the study performed by Kim et al. [5] regions with the greatest heat transfer and thermal performance were dictated by rib angle of attack and the ratio of rib to rib pitch and rib height. From this study, the highest heat

transfer value was found at $\alpha = 53.31$ degrees and $p/e = 6.5$. The greatest heat transfer and thermal performance were found to be within the ranges of 50 deg $\leq \alpha \leq$ 60 deg and $6.0 \leq p/e \leq 7.0$.

From Gupta et al. [6]'s review of gas turbine blade internal cooling configurations, it is apparent that numerous rib configurations have been explored including orthogonal ribs, angled ribs, v-shaped ribs, and combinations of ribs and grooves within channels. Within this study, only orthogonal and angled turbulators were explored as current industry practice typically utilizes these configurations for ease of manufacture. Han et al. [7] studied heat transfer augmentation of ribbed channels through analysis of Nusselt number ratios of ribbed and smooth walls with respect to varying rib angle of attack. Within this study, rib angles tested included 45^o, 60^o, and 90^o of various configurations. Nusselt number was related to friction factor ratios. Results of this study showed that improvements angled ribs provided better heat transfer augmentation when compared to parallel (90^o) rib configurations. In addition, it was found that parallel angled rib configurations outperform crossed rib configurations provided better heat transfer performance with regards to turbine cooling.

2.2.2 Pin-Fin Arrays

As current trailing edge configurations containing pin-fin arrays utilize cylindrical pins because they are easily manufactured, the current study focused on cylindrical pins. A pin-fin within a nozzle guide vane is typically a cylindrical extrusion between the pressure side and suction side surfaces within the trailing edge region. The purpose of a pin is to increase the surface area on which a part can be cooled. Pins are oriented perpendicular to the flow direction to maximize forced convection across the pin surface. An array of pins consists of numerous pins that are oriented inline or staggered with respect to the streamwise direction of flow. Within a turbine operation, the pins within an array will draw heat from the external surface of the airfoil to the internal cavity where cooling air will draw the heat away from the pins to be expelled from the part. Wakes shed by each pin increase free stream turbulence and the boundary layer development over the pin-mounted surface is disturbed [3]. Flow disturbance caused by the formation of a horseshoe vortex just upstream of the stagnation region of the pin also induces heat transfer via flow disturbance.

Heat transfer within pin-fin array arrangements has been extensively researched. Within this research, a predominant number of studies have focused on normalized dimensional parameters of pin arrangements based on the diameter of the pins. These parameters include height-to-diameter ration (H/D), spanwise spacing of pins normal to the coolant flow direction (S/D), and streamwise spacing in the flow direction (X/D). As observed by Lau, et al. [8], pins utilized within gas turbine engines typically displayed a pin height to diameter (H/D) ratio between one half and four. Within [9], [10], and [11], it was found by VanFossen et al. that heat transfer improves for H/D > 3 within increasing H/D. However, it was also found that heat transfer differences are minimal with varying H/D for H/D < 3.

Metzger et al. [12] evaluated the effects of spanwise and streamwise spacing within pin fin arrays. This research observed that decreasing both spanwise and streamwise spacing induced higher turbulence within the channel and increased heat transfer but resulted in higher pressure losses throughout the pin fin array. In addition, this study observed that heat transfer augmentation levels off beyond a certain row of pins. Lyall et al. [13] and Lawson et al. [14] examined Reynolds number, spacing, and H/D effects on heat transfer for pins and pin fin arrangements. Both studies found that heat transfer increased due to higher turbulence levels within the channel as a result of higher Reynolds number flow and decreased spacing between the pins. Heat transfer augmentation was found to be increased at low Reynolds numbers when compared to higher Reynolds numbers due to larger conductive effects on the pins.

2.3 Microchannels

As noted by Liu et al. [15], the reasoning behind the effectiveness of microchannels can be derived from the definition of Nusselt Number, shown in Equation (1) below:

$$Nu = \frac{hD_h}{k} \tag{1}$$

By definition, Nusselt number (*Nu*) is the ratio of convective to conductive heat transfer at a boundary. Its parameters are the convective heat transfer coefficient *h* at the boundary, the hydraulic diameter of the channel D_h which is taken as the characteristic length of the microchannel, and thermal conductivity of the convective fluid *k*. If Nusselt number is held constant for a given system, as D_h decreases, the internal heat transfer coefficient within a

microchannel will increase if the fluid is assumed to be at a constant thermal conductivity. Due to the small size of the channel, the increase in h is on the order of magnitude of 10^3-10^6 depending on the size of the channel [15]. Because microchannels have large amounts of surface area per unit volume, this type of cooling configuration has been investigated for use as compact heat exchangers in a variety of applications [1].

Within microchannel cooling, surface roughness plays a significant factor within channel heat transfer and fluid flow given the small size of the channel. Surface roughness effects within microchannels were explored by Weaver et al. [16] with respect to heat transfer and pressure drop within the channel. Parameters varied within the analysis included microchannel manufacturing method, average surface roughness, maximum surface roughness, and channel height. Within this study, Nusselt number and friction factor were analyzed across a range of Reynolds numbers of $5000 < Re < 40000$ at known thermal and fluid conditions. Results of the study indicate that when channel roughness approaches 2.2% of the channel height, there is an effect on heat transfer augmentation. However, the study also concluded that pressure losses within the channels exceed the heat transfer benefit provided.

Snyder et al. [17] performed a study on dimensional tolerance and surface roughness within additively manufactured circular microchannels. This particular study explored the effect of build direction on these parameters within a direct metal laser sintering process. Test articles were built using either a vertical, horizontal, or diagonal build direction and measurements of inscribed and effective diameter, total runout, concentricity, circularity, and average surface roughness were made for each circular channel. A vertical build was defined as pieces in which the build direction was in the direction of the channel length. A horizontal build was defined as pieces in which the build direction was normal to the channel length. A diagonal build was defined as pieces in which the build direction was at 45^o relative to the central lengthwise axis of the channel. The study found that vertical builds produced the highest quality channels and lowest inherent surface roughness. Diagonal and horizontal build directions were found to be induce high surface roughness within the channel. These trends are important to note when designing additive microchannels as the build direction of the channels will play a significant factor in heat transfer augmentation and channel pressure drop.

Kirsch & Thole [18] explored heat transfer and pressure loss performance of

additively manufactured wavy channels at engine relevant Reynolds numbers. Microchannel cooling features of specified wavelengths were manufactured utilizing Direct Metal Laser Sintering. Results within testing displayed high pressure losses within the wavy microchannels without additional heat transfer augmentation induced flow structure promoted by the waves. However, findings from the study indicate that good heat transfer performance with minimal pressure loss could be found in larger wavelength microchannel configurations.

Zhang et al. [19] explored the design and optimization of microchannel heat transfer systems. Two different configurations of multiple microchannel heat sinks were studied; straight and U-shaped channel designs. Various responses to represent the influences of flow rates and geometrical variables on the heat transfer performance have been parametrically modeled and studied. Findings of the study indicate that geometry of the channels strongly influences the pressure required for flow, and that narrower channels lead to greater channel pressure. In addition, thermal resistance was found to decrease with increasing flow rate and with greater contact area. The results indicate that the convective heat transfer coefficient will increase with increasing flow rate within microchannel systems as convective resistance is defined as the reciprocal of the convective heat transfer coefficient multiplied by the channel internal surface area.

Morini [20] provides a sound review on the convective heat transfer through microchannels across available literature. Condensed findings from this review include the following with respect to Nusselt number for single-phase flow of microchannels: In the laminar regime, the Nusselt number decreases with increasing Reynolds number. Within the turbulent regime, the Dittus–Boelter correlation and the Gnielinski correlation require correction for use within microchannel fluid flow. High surface roughness of the walls relative to the size of the channel exhibits increases in convective heat transfer within microchannels. In addition, variation of viscosity with the temperature affects the heat transfer within a microchannel.

As a follow-up to [20], Morini & Yang [21] provides an overview of the determining factors of Nusselt number in microchannels. Experimental data and the published results highlight the characteristics of convective heat transfer for both liquids and gases through microchannels and provide guidelines for interpretation of the experimental results. An experimental campaign is proposed to analyze convective characteristics of liquid and gas flows

in microchannels. This campaign consists of an a priori analysis of the presence of scaling and micro-effects and the coupling of a numerical modeling of the complete test rig to the experimental analysis [21].

2.4 Uniqueness of Research

Although research has characterized microchannels from multiple performance aspects including heat transfer characterization, pressure drop characterization, channel design, surface roughness effects on heat transfer and fluid flow, implementation of microchannels into specific turbomachinery component cooling applications has not been explored. Testing has been performed primarily on component geometries that do not mimic those represented within a nozzle guide vane. Therefore, in order to gain a better perspective on the benefit of implementing these cooling geometries into a trailing edge configuration, testing was performed utilizing a test article that reflects the geometry of a nozzle guide vane trailing edge.

This study presents a comparative analysis between microchannel cooling, pin fin arrays, and rib turbulators within a uniform trailing edge geometry. Although each cooling configuration has been studied at length with respect to heat transfer performance on an individual basis, few studies attempt to draw direct comparisons between these configurations. The emphasis of this study is on the implementation of each cooling configuration into an identical trailing edge geometry to simulate comparative evaluation necessary for successful trailing edge cooling design.

Chapter 3: Experimental Methodology

3.1 Test Article Design

Each cooling configuration was tested within a uniform trailing edge geometry as shown below in Figure (**7**). The external geometry of each test piece was identical: only the internal geometry varied.

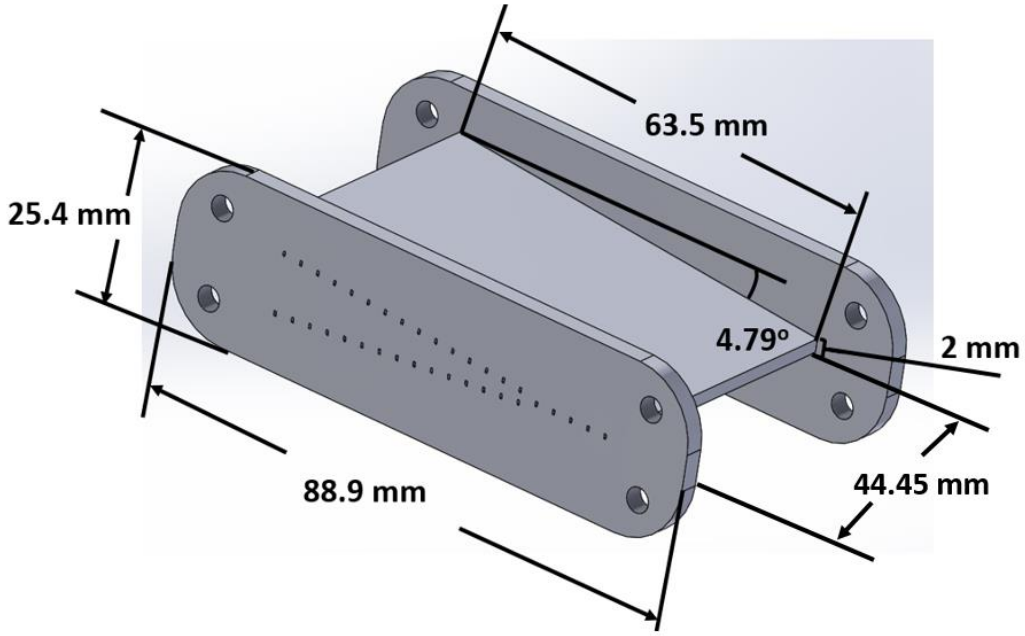

Figure 7: Dimensioned test article geometry

Figure (7) displays the dimensioning of the trailing edge configuration for each test article as derived from [22]. The test articles utilized in the current study were scaled down from those presented in [22] to allow higher resolution imaging of the external surface while testing. The test articles were manufactured in Accura 25, a polyethylene-like material, on a ProJet 7000 HD 3D printer. Components were printed by Quickparts, a subdivision of 3D Systems. A design for each of the three cooling configurations was placed within the geometry shown in Figure (**7**) for comparative testing.

Within the design of these components, it is important to note the limitations, material properties and tolerances inherent to additively manufactured components. A high-resolution printer was used to manufacture the test articles used within the current study. Within the manufacturing process, printing tolerances specified by Quickparts were +/- .01inches for the first

inch of the build with respect to the build platform. After the first inch, an additional tolerance of +/- .002" was specified for every inch thereafter. From visual inspection and caliper measurements, internal cooling features within the components adhered to the specified design. Post processing of the test articles was necessary to account for thermal shrinkage of each part and ensure the bolted flange mate between the test article and each plenum. Within the pin-fin array internal cooling cavity, support structures between the internal wall surface and the pin were removed upon receipt of the test article using a rigid wire. As a result, a non-uniform pin geometry and defect on the wall were present at the location of these support structures. Upon the external face of the flanges on all components, clearance holes required additional material removal for sealing bolts to properly align with the inlet and outlet plenums. These alterations did not affect internal cooling features within the test article but did decrease the thermal mass of each component.

Material properties of Accura 25 provided by the manufacturer are listed in Table 2 below.

Table 2: Material Properties of Accura 25

Material Property	Value	Units
Thermal Conductivity	0.2 - 0.4	W/m-K
Specific Heat Capacity	1.2 – 1.4	J/(g-^{o}C)
Heat Deflection Temperature (@ 66 psi)	136 - 145	^{o}F
Solid Density @ 77 ^{o}F	1.19	g/cm^{3}

Due to the anisotropic nature of material properties of additively manufactured components and the uncertainty regarding the build direction specified within the manufacturing of each test component, mean values of thermal conductivity and specific heat capacity were calculated from Table 2 and used in this analysis. Therefore, the thermal conductivity and specific heat capacity of the material were assumed to be 0.3 [W/m-K] and 1.3 (isn't 1.3 the mean) [J/(g-K)], respectively. By using a mean value, comparing the different test pieces could be done with less variables. Thermal conductivity and specific heat capacity values were specified to be measured at room temperature, which was assumed to be 25^{o}C. Heat deflection temperature, was utilized as

a benchmark for which the flow temperature setting at the heater was dictated. Heat deflection temperature is the temperature at which a solid will deform under the influence of a heat load.

Figure (8) below displays the internal cooling configuration for the microchannel test article.

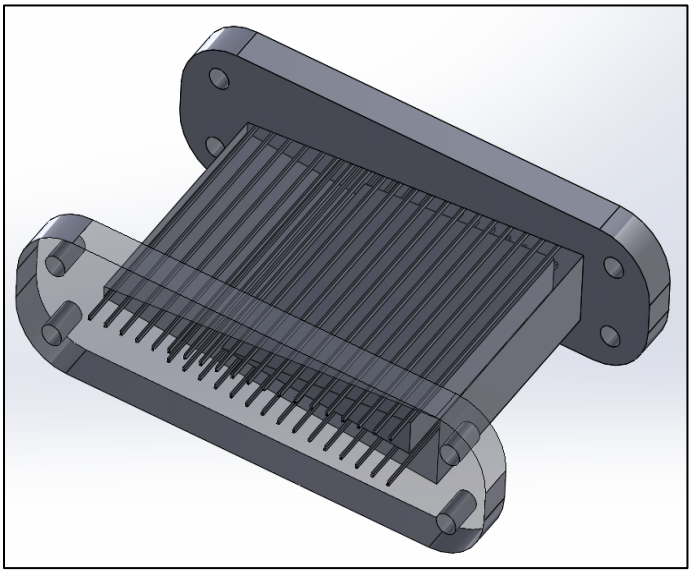

Figure 8: Microchannel test article internal cooling features

Fifteen rectangular microchannels span each side of the trailing edge with a pitch of 3 mm, 1.05 mm below the surface. Five microchannels were placed in a chord-wise plane in the trailing edge of the test article. Each rectangular microchannel has a hydraulic diameter of 500 µm. The hydraulic diameter of each microchannel was calculated using Equation (2) below:

$$\boldsymbol{D_h = \frac{4A_{cs}}{P} = 4\left(\frac{(0.375 * 0.750)[mm^2]}{(2 * 0.375\,[mm] + 2 * 0.750\,[mm])}\right) = 500\mu m} \quad \textbf{(2)}$$

The width of each channel is 375 µm and the channel height is 700 µm. To minimize thermal mass associated with the microchannel configuration, an uncooled cavity was placed within the microchannel cooling test article. Each microchannel spans the 50.8 mm length of the test article. A notable difference between the microchannel test article and both the pin array and ribbed turbulator test articles was an additional 1/8" thickness added to the thickness of the plenum mount flanges. This additional material was added following flange cracking in preliminary tests. This change in thickness was accounted for within positioning of the test article within the experimental apparatus discussed in Chapter 3 Section 2 of this document.

Within the ribbed turbulator array test article shown in Figure (9) below, each rib has a height (*e*) and width (*w*) of 0.5 [mm]. The test article contains 52 total ribs divided equally between the upper and lower surface of the cooling channel across the channel span in a staggered configuration. Following the study performed by Kim et al. [6], the rib angle of attack (α) was taken to be 53.31 degrees with respect to the direction of fluid flow within the channel. The rib angle of attack is defined as the angle of the rib with respect to the spanwise direction of the channel. The ratio of rib to rib pitch and rib height (*p/e*) was 6.5.

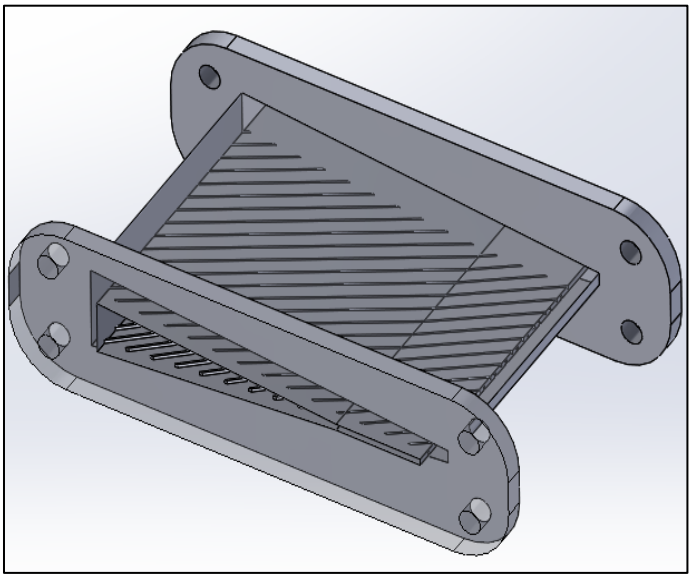

Figure 9: Ribbed Turbulator test article internal cooling features

Within the pin array test article shown in Figure (10), each of the 33 pins has a diameter (D) of 4 mm. This piece contains a staggered pin array with 5 rows. The number of pins per row in the streamwise direction alternates between seven and six. The pins have a streamwise spacing of X/D = 2 and a spanwise spacing of S/D = 2. The height of an individual pin spans the thickness of the internal cooling passage at a 90^{o} angle relative to the direction of flow. The range of values H/D varies from 2.159 to 0.157 by pin location relative to the spanwise direction S with changing channel height. As shown within [13 & 14], more dense arrays displayed better heat transfer augmentation at lower Reynolds number flows.

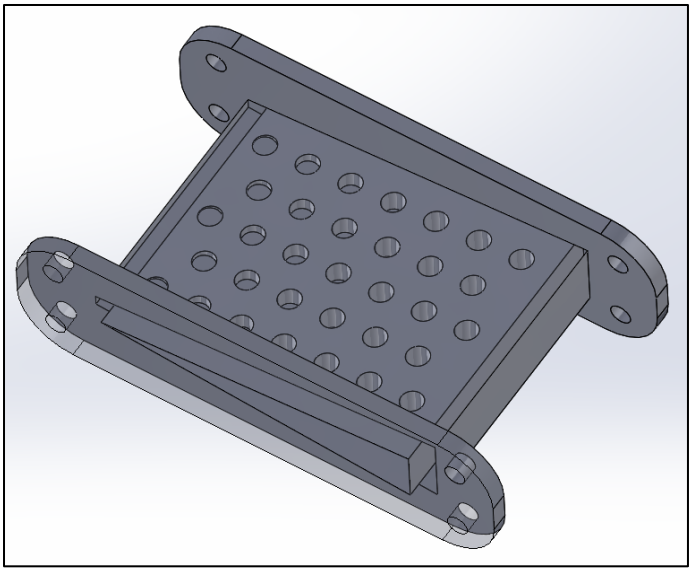

Figure 10: Pin Array test article internal cooling features

3.2 Experimental Facility

To evaluate these parameters, the test apparatus displayed in Figure (11) below was utilized to test each cooling configuration.

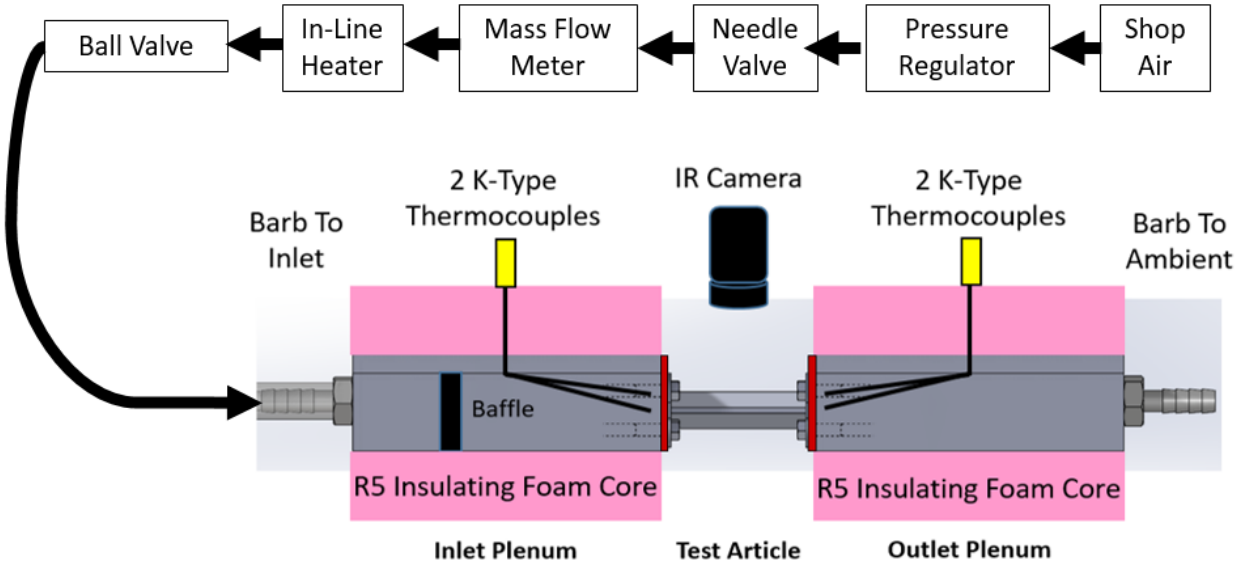

Figure 11: Experimental test facility schematic

Air supplied by the on-site compressor was regulated utilizing a ball valve (for bulk regulation) and a needle valve (for fine-tuned regulation) prior to mass flow measurement ($\dot{m}$). The air is heated to a temperature of 120 ^{o}F with an Omegalux AHP-5051 120VAC in-line air heater. Once flow reaches the desired steady state temperature, it is directed into the inlet plenum via a ball valve through an insulated tube. To minimize the heat lost by the mass flow entering the plenum, the tube was wrapped in a single layer of R5 insulation and covered by three additional layers of insulating foil tape. Upon entering the inlet plenum, the air passes through a baffle to ensure plenum conditions are met prior to entry of flow into the test article. The temperature of the air within the inlet plenum (T_i) is measured with two K-type thermocouples. The thermocouples were placed just upstream of the test article flow channel(s) entry at two positions shown in Figure (12) below. Within Figure (12), the inlet region of the test piece exposed to the plenum is outlined with a red border.

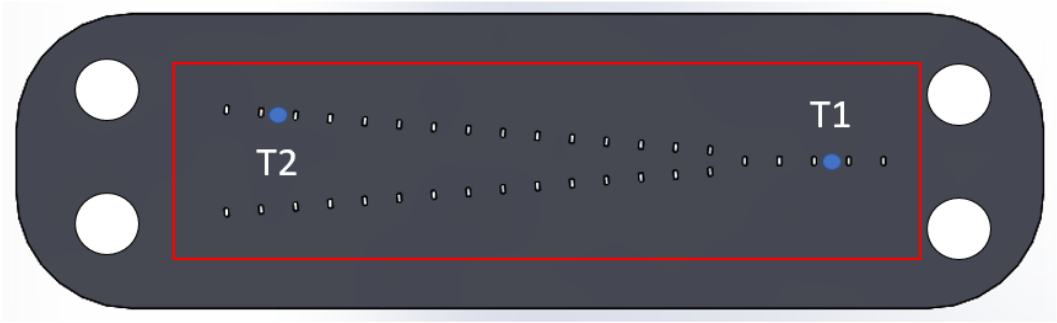

Figure 12: Thermocouple Position within the Inlet Plenum relative with respect to channel inlet region

Thermocouple (T3) and thermocouple (T4) were placed just aft of the microchannel test article within the outlet plenum, mirroring the positions of T1 & T2. These positions were chosen to adequately capture the span-wise temperature of the mass flow near the test article-plenum interface

Surface temperature on the outer surface of the test article is measured over time with a FLIR A325sc infrared camera. This infrared camera has an accuracy of +/- 2% of the measured value and a resolution of 320 x 240. This camera is located normal to the upward facing surface of the test article at a distance of 0.3 meters from the measured face. This distance is within the focal range of the camera. To ensure optimal viewing of surface temperature, the upper surface of

the test article was covered with a uniform layer of black paint with an estimated emissivity of 0.95.

Cooled air exits the test article into a plenum where fluid temperature (T_o) is measured via two K-type thermocouples. Fluid then exits the test article into ambient outside of the test article enclosure. To minimize heat losses within the plenums, 1" thick R5 foam board insulation surrounds each plenum. To inhibit outside radiation from affecting temperature measurements, the entire test apparatus is housed in an opaque box.

3.3 Procedure for 3D Inverse Transient Conduction Analysis

The testing method utilized within this study stems from the Thermal Inertia Heat Transfer Coefficient technique pioneered by Nirmalan et al. [23] for use in quantifying full-surface internal heat transfer coefficient distribution of turbine airfoils. This method utilizes transient IR data taken within component testing to create a mapped surface boundary condition for a finite element model of the part geometry. Full surface internal heat transfer coefficients for each position on the surface are found by iteratively updating internal heat transfer coefficients until convergence of measured and predicted external wall temperatures is reached for the desired transient time interval. A flow chart outlining the derived analysis process utilized within this study can be found in Figure (13) below.

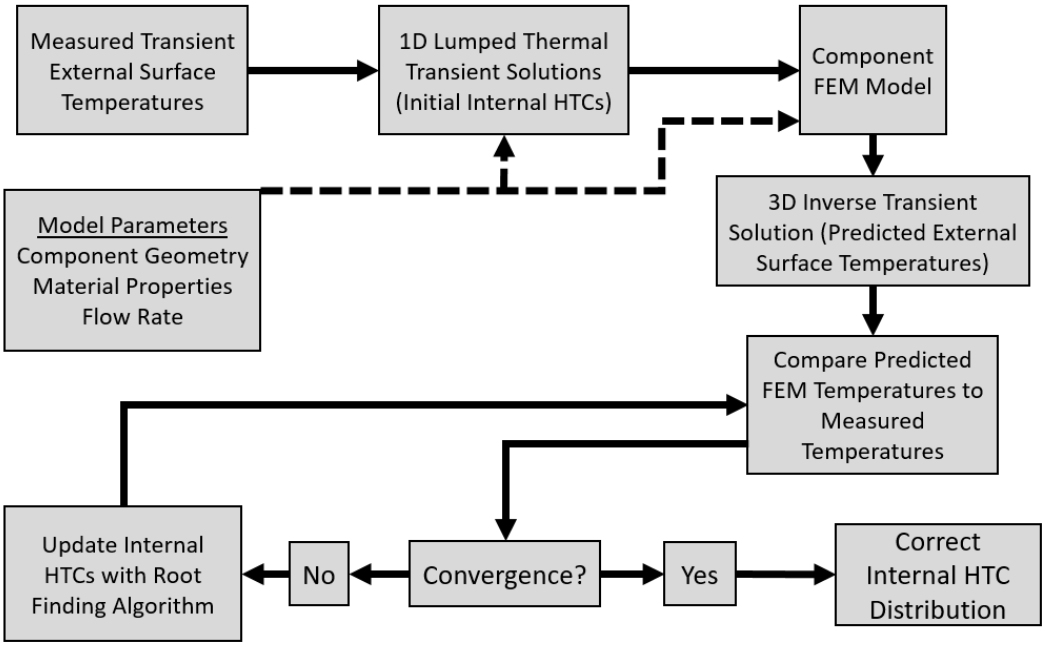

Figure 13: Analysis process for determining internal heat transfer coefficient from [2]

Prior to testing, the test article is confirmed to be isothermal via a 5-6 hour cooling period between conducted tests. Preliminary surface temperatures are then measured utilizing the infrared camera. Temperature measurements taken from the upstream and downstream thermocouples (T1-T4) to confirm steady state plenum conditions prior to testing. The surface temperature range displayed by the IR camera is also checked against the measured temperature within the room. The range of room temperatures within the testing space was determined to be between 65 ^{o}F and 73 ^{o}F throughout testing. Room temperature at the start of each test was recorded. During the confirmation of initial thermal state, air supplied to the system is heated to a constant temperature of 120^{o}F and mass flow is regulated to match a desired Reynolds number (why did we decide to match Re?). Within this study, the mass flow utilized within each test was regulated in an attempt to create similitude about set Reynolds numbers for component tests. Reynolds numbers selected for testing were 800, 1200, 2300, and 3000. These values were selected to evaluate the heat transfer performance of each configuration at lower mass flows. Once initial test conditions are confirmed, flow is directed into the test article and a controlled thermal transient is induced at $t = 0$.

During the transient, the infrared camera records the external temperature distribution of the test article outer surface to acquire $T_s(x, y, z, t)$. Over the testing period, the thermal response data is stored at each position on the surface for every time step of the transient. Transient measurements were taken over a duration of 60 seconds at a frame rate of 30 Hz. Consecutive temperature profiles can be utilized to construct a transient thermal history of the test article for use in determining internal heat transfer coefficients at each position. As a single camera is used, a two-dimensional image will be collected and transformations must account for the three-dimensional geometry of the part. Figure (14) below shows the orientation of the coordinate reference system used within the FEM model for heat transfer coefficient analysis.

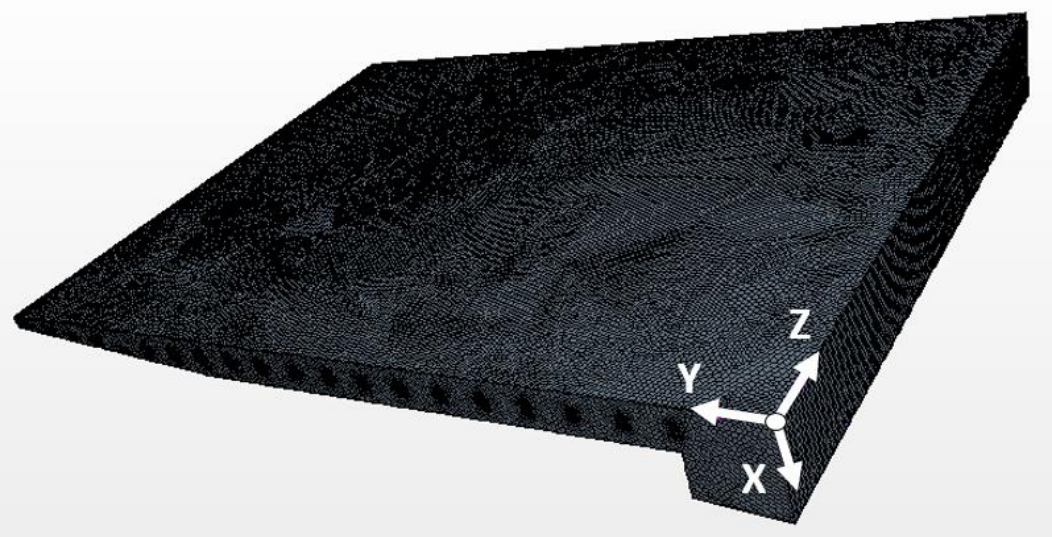

Figure 14: Orientation of the Coordinate Reference System of the finite element model within STARCCM+

Due to alignment of the camera in a plane normal to the measured surface, position *x* is taken to be zero at every pixel within the measured temperature profile. Position *y* within each image corresponds to the spanwise position on the test article. Position *z* within each image corresponds to the streamwise position on each test article. Due to the positioning of the camera, temperature profile data exported by the camera required additional manipulation to ensure the mapped temperature profile imposed as a mapped surface boundary condition consisted only of pixels corresponding to the surface of the test article. Comma separated values (.csv) files exported from the IR camera were post processed in MATLAB utilizing the script within Appendix A3. This method of manipulation utilized the 'ginput()' function within MATLAB to allow the user to

pick the corner points of the test article from a test image collected near the end of the transient. Utilizing these points, data from pixels within the selected bounds are saved to a .csv file containing *x*, *y*, *z*, and temperature data at each point on the test article surface.

Differentiation between the test article surface and the outer surface of the flange with respect to streamwise position (*z*), as well as distinction of the test article surface boundary in the spanwise direction (*y*), were determined by notable temperature differences at interfacing points. One concern of the method of selection was ensuring repeatability when selecting points on the same test article between tests. This was particularly evident for low Reynolds number test cases where the difference in temperature between the test article and ambient was small. To reduce possible error and aid in selection of the corner points, the temperature bounds on the generated contour plot were manually adjusted to allow for greatest possible differentiation between neighboring pixels.

As the process of determining full surface internal heat transfer coefficients requires iteration, it is suggested within [23] that an initial guess for the internal surface heat transfer coefficients is made utilizing a lumped thermal capacity model in Equation (3):

$$\frac{T_s(t) - T_{initial}}{T_{coolant} - T_{initial}} = e^{-\left(\frac{h}{\rho L_c c_p}\right)t} \tag{3}$$

Within this model, L_c refers to the thickness between the internal surface of the wall and the measured surface for each test article. $T_{coolant}$ is taken as the average of measured temperatures at the entrance of the test article ($T_i(t)$). $T_{initial}$ is the recorded temperature of the surface when $t < 0$. Density (ρ) and specific heat (c_p) are inherent properties of the air utilized for convection. Assumptions inherent to this model include spatial uniformity of temperature at any instant in time, an insulated external wall and negligible thermal resistance due to conduction through the wall thickness with respect to internal convective heat transfer [24]. Although these assumptions are not true for the present system, use of this model allows for a reasonable initial solution for use in iteratively solving the three-dimensional model in some cases. The purpose of using lumped capacitance analysis to generate an initial guess for internal heat transfer coefficient was to reduce time taken to reach convergence within the heat transfer model.

Although the work presented within [23] utilized lumped analysis to provide preliminary guesses for internal heat transfer coefficient, the present study found the use of a constant value of 50 [W/m^2-K] as the specified internal heat transfer coefficient across the internal surface to be satisfactory for use within the model. This was proven through the achievement of identical reported values of internal surface average heat transfer and average temperature of the external surface within two separate test cases. Within iterations of the model, it was also found that the use of the lumped capacitance solution created minimal difference in the time required to reach the solution for the models. Because the use of a constant value for internal heat transfer coefficient across the internal surface reduced the complexity of the model iteration, 50 [W/m^2-K] was specified as the initial guess for internal heat transfer coefficient for all simulations.

Utilizing STAR-CCM+ via the Oakley supercomputer [25], a finite element model (FEM) was generated from SolidWorks-generated IGES part geometries of each test article and embedded with the specified values of solid density, thermal conductivity, and specific heat capacity discussed previously for Accura 25. The imposed initial temperature condition on the model was set to the average surface temperature of the test article at isothermal condition prior to testing. To reduce the number of cells necessary to define the mesh for each test article model, components were modeled utilizing a sectioned model taken about the central axis of the test article and a symmetry boundary was imposed upon surfaces that lay in-plane with the symmetry axis. Figure (15) below displays the surfaces on which boundary conditions were defined on each model.

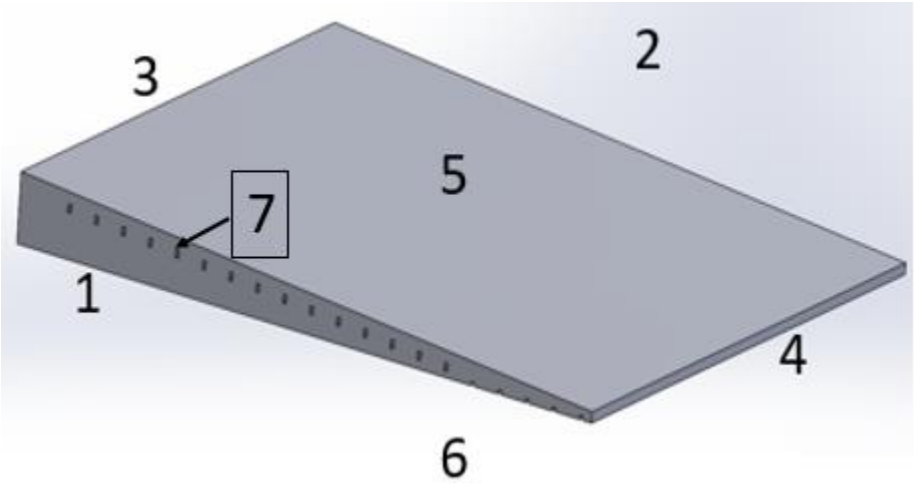

Figure 15: Defined surfaces within component FEM models (Microchannel configuration shown)

Within Figure (5), the numbers depicted indicate the external surfaces of each test piece. Table 1 below provides a listing of the boundary conditions associated with the model surfaces listed in Figure (5).

Table 3: Description of surfaces and applied thermal boundary conditions within the Inverse Heat Conduction model

Surface	Description	Model Boundary Conditions
1	Inlet	Adiabatic Wall
2	Outlet	Adiabatic Wall
3	Forward Boundary of Trailing Edge Region	Adiabatic Wall
4	Trailing Edge	Adiabatic Wall; Assumed $T_s(t)$ of Trailing Edge Section Surface 5
5	Viewed Surface	Measured $T_s(t)$
6	Non-viewed Surface	Imposed symmetry with Surface 5 about mid-plane
7	Internal Cooling Cavity	Convection; HTC specified per output of previous model iteration

The inlet and outlet regions (Surfaces 1 & 2) are specified as adiabatic surfaces due to the inability to accurately predict heat transfer on the surface. Although convection heat transfer is applied to the surface of the test article connected to the plenum, this surface is removed from the mapped region in the streamwise direction by the thickness of the flange. Because flange thickness between test articles varied within testing, it is difficult to determine the effect of convection on the test article surface from the plenum with the current test apparatus. The purpose of the adiabatic boundary condition is to provide a uniform parameter at which to analyze each system

and reduce bias within the analysis between the heat transfer model. The error caused by this definition will be explored within future models. A methodology to determine the effect of heat transfer from the plenum/test article interface will be explored within future testing. The forward external wall (Surface 3) is considered to be an adiabatic wall within testing as it is well insulated with 1" thick R5 foam core insulation across the entire surface. The trailing edge region (Surface 4) was specified as an adiabatic wall to aid in simplification of the model. However, due to the small thickness of material at the trailing edge (2 mm), it is assumed that the temperature of the trailing surface can be accurately represented by the temperature of the measured surface at the interface of the measured surface and the trailing edge. The boundary condition on the viewed surface (Surface 5) is imposed via a Data Mapper within STAR-CCM+ containing the temperature profile of the measured surface extracted from the model. Table (4) below provides a list of the time steps at which temperature profile data was taken for use within the mapped boundary condition.

Table 4: Time step of IR temperature profiles selected for use as mapped boundary condition within 3D inverse heat conduction model

Model	Flow Reynolds Number	Time Step (s)
Pin Array	800	60.0
	1200	30.0
	2300	30.0
	3000	30.0
Microchannels	800	60.0
	1200	30.0
	2300	30.0
	3000	30.0
Ribbed Turbulators	800	60.0
	1200	30.0
	2300	30.0
	3000	36.6

The last time step within the transient was selected to be the mapped condition for tests at Re = 800 to ensure ease of convergence within the model solution. At earlier time steps within these test, minimal temperature difference appeared to cause divergence within the model. Within the ribbed turbulator model at Re = 3000, the data from the 36.6 second time step was chosen as the mapped boundary condition on Surface 5 due to irregulates within the mapped temperature condition at the 30 second time step. For all other models, the midpoint of the transient was chosen to reduce time taken to reach convergence within the model. The non-viewed surface (Surface 6) was simulated within the model by a symmetry boundary condition imposed at the central axis of the test article to account for the mirrored geometry of the test article about this surface. When applying the boundary condition for the non-viewed surface, it was important to note that the ribbed turbulator test article contains staggered ribs on both the upper and lower surface of the internal cooling channel. Further testing will be conducted to confirm the validity of this assumption for this surface. The surfaces of internal cooling channels within each model were specified by convection boundary condition.

The three-dimensional model is first executed with the application of the applied boundary conditions to predict the temperature distribution on the external surface of the test article for the first guess of internal heat transfer coefficient. The transient conduction period within the model matches the data collection period during testing. Time steps of the model were refined as required to ensure convergence of the heat transfer model. Output from the model is then compared to the transient temperature profile of the measured surface at every node to determine convergence via an established parameter for allowable ΔT. A field function within the model was generated to act as the root finding algorithm for which convergence of the model is determined. From [23], the root-finding algorithm chosen within the present models was chosen to be Equation (4).

$$\frac{T_{s,measured}(y,z,t) - T_s(y,z,t=0)}{T_{s,predicted}(y,z,t) - T_s(y,z,t=0)} \tag{4}$$

Utilizing this root-finding algorithm, the internal heat transfer coefficient was iterated utilizing Equation (3) below:

$$h_{n+1} = h_n\left(\frac{T_{s,measured}(y,z,t) - T_s(y,z,t=0)}{T_{s,predicted}(y,z,t) - T_s(y,z,t=0)}\right) \tag{5}$$

If convergence is not achieved, additional iterations are performed until the stable root-finding numerical algorithm has an average output across the measured surface near one and the predicted temperature profile matches the measured surface temperature within 1%. Once convergence is achieved at a single mesh size, convergence is verified by attaining convergence for the same model at a refined base mesh size. Two criterion must be satisfied in order to confirm convergence of the model. The first criterion for convergence is that the predicted temperature profile produced by the model matches the mapped surface temperature within a percent difference of 1%. The second criterion established to confirm convergence was that the converged internal heat transfer coefficients at a single base size converge with the value of internal heat transfer coefficient at the refined mesh size within a percent difference of 5% between values. Uncertainty within this measurement is driven by the uncertainty within measurements taken from the infrared camera. Accuracy of the camera is used within testing is +/- 2% of the measured value. Therefore, through calculation of the uncertainty inherent within Equation 4, the uncertainty of each calculated value of internal heat transfer coefficient is +/- 8%.

Chapter 4: Results

4.1 Bulk Flow Analysis

Bulk flow analysis was performed to evaluate the convective heat transfer rate within each test article at the time step analyzed. Although bulk flow analysis is typically performed to evaluate heat transfer of a component at steady state, it was used in the present study to establish a baseline on which the thermal inertia heat transfer coefficient method could be performed. Measurements from bulk flow analysis used within the implementation of the 3D inverse heat conduction models included plenum temperature at the inlet and outlet. The governing equation for convective heat transfer rate for bulk flow is shown in Equation (6) below as defined in [24]:

$$q = \dot{m} c_p (\bar{T}_{inlet} - \bar{T}_{outlet}) \tag{6}$$

Mass flow rate ($\dot{m}$) varied for each test. The average inlet temperature ($\bar{T}_{inlet}$) was taken as the average of measurements produced by the thermocouples positioned in the inlet plenum (T1 and T2) at each time step. The average outlet temperature ($\bar{T}_{outlet}$) was taken as the average of measurements produced by the thermocouples positioned in the outlet plenum (T3 and at each time step. The difference between the value of T3 and T4 varied depending on both the Reynolds number at which tests were conducted and the test article. For the microchannel configuration, measurements between tests were relatively close given the relatively even distribution of the convective fluid flow throughout the test article. For both the pin-fin array and ribbed turbulator test articles, T3 displayed a lower temperature value than T4 throughout each transient as convective fluid flow maintained a bias toward the forward region of the test article in which T4 resided. As mass flow increased within testing of these two components, the difference between the temperatures measured between T3 and T4 increased. The specific heat of the convective fluid (c_p) was defined for the air based on the average of the inlet average temperature and the outlet average temperature. Figures (16-19) display heat transfer rate as a function of time for each tested case. Data extracted within testing of the pin-fin array is shown in red. Measurements taken from testing of the ribbed turbulator are displayed via the black lines. Microchannel measurements are conveyed using the blue lines. These measurements define the amount of heat being extracted over time at specified Reynolds numbers for comparable evaluation.

Figure (16) below contains data for each configuration at a Reynolds number of 800. Flow at this Reynolds number is within the laminar regime for all cases. At this flow regime, microchannels exhibit the lowest heat transfer among tested configurations. The pin-fin array exhibits the highest heat transfer at this regime, nearly doubling that shown by the microchannel. This is likely due to the pins experiencing the largest induced turbulence at this flow regime.

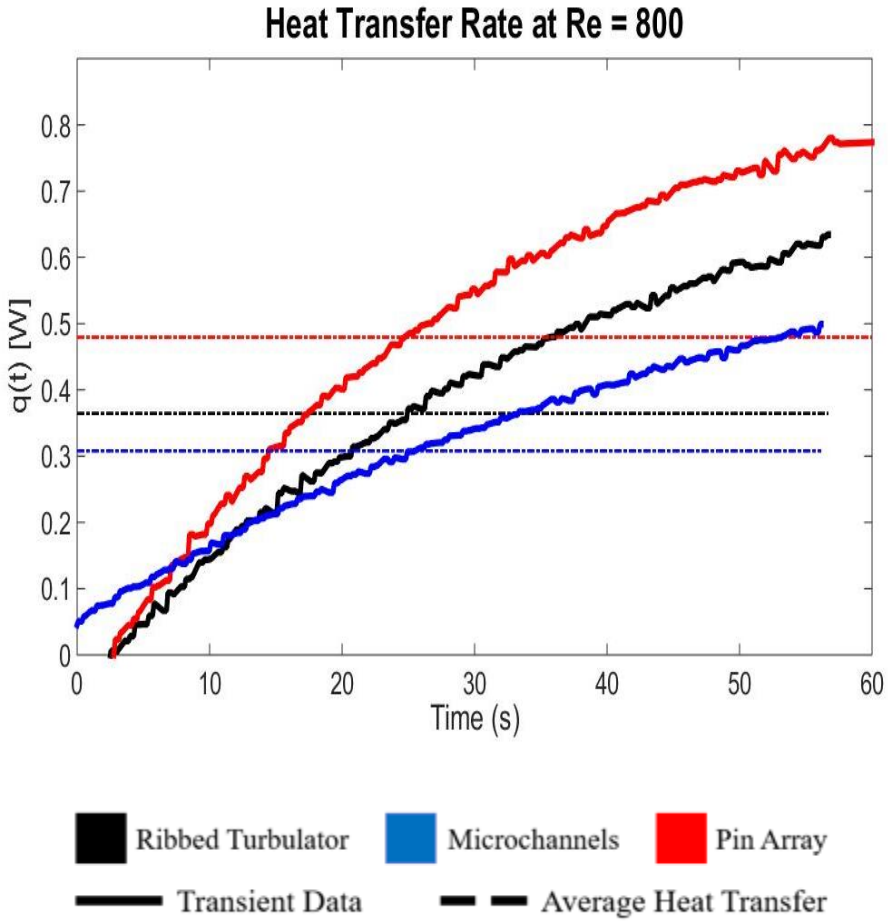

Figure 16: Bulk flow analysis heat transfer rate at Re = 800 for each cooling configuration

Within Figure (17), heat transfer rates are shown for the test cases taken at a Reynolds number of 1200. It is within this flow regime that microchannels begin to display effective heat transfer across the entire test article, and not just at the inlet region. Within this flow regime, the pin-fin array again displays the best heat transfer rate among configurations test. However, the microchannel configuration displays slightly better convection heat transfer in this case when compared to the ribbed turbulator.

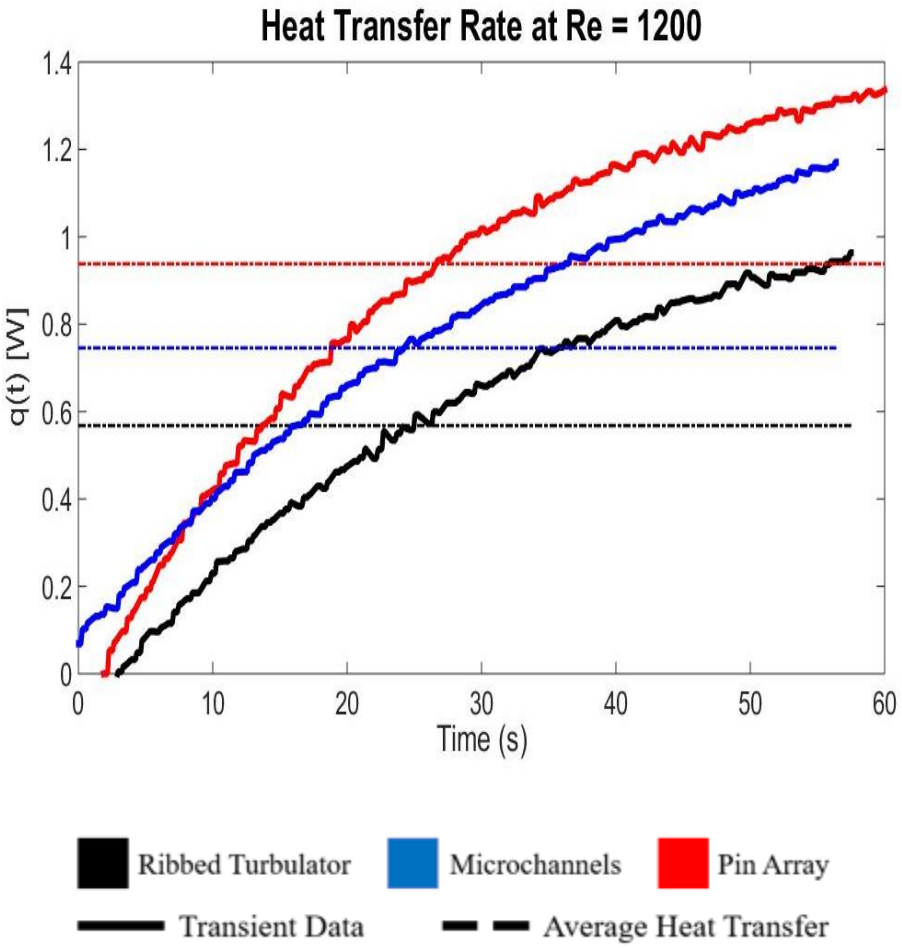

Figure 17: Bulk flow analysis heat transfer rate at Re = 1200 for each cooling configuration

Figure (18) displays bulk flow analysis data for a Reynolds number of 2300. Within this regime, the pin-fin array begins to reach steady state heat transfer at approximately the 40 second time step. The ribbed turbulator exhibits notable heat transfer benefit at within this region. Within this flow regime, microchannels exhibit the lowest heat transfer among all configurations tested.

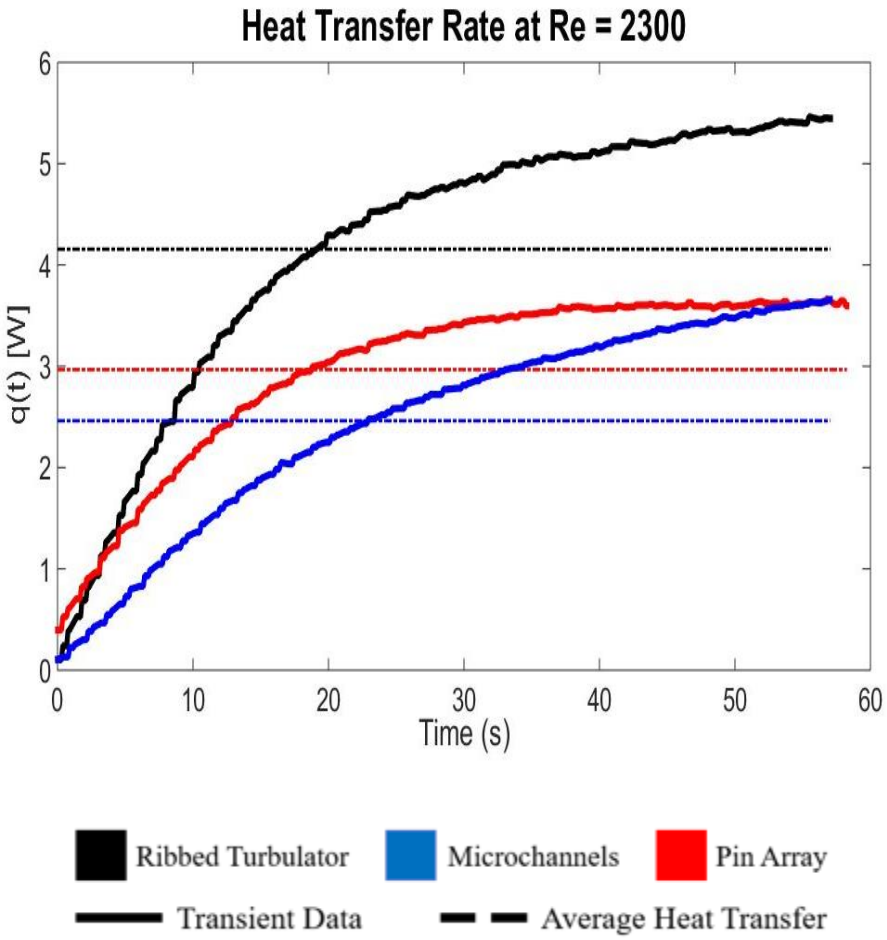

Figure 18: Bulk flow analysis heat transfer rate at Re = 2300 for each cooling configuration

Figure (19) displays the results of bulk flow analysis from tests conducted at a channel Reynolds number of 3000. At this flow regime, the final value shown within the transient for all cases is nearly uniform. However, both the ribbed turbulator configuration and the pin-fin cooling geometry reach a steady state heat transfer value at the end of the transient time period. From this data, it is reasonable to suspect that the microchannel still has potential for a higher heat transfer rate at steady state within this flow regime. Further tests will be required to confirm this assumption and explore conclusion as it relates to this, and more turbulent flow regimes.

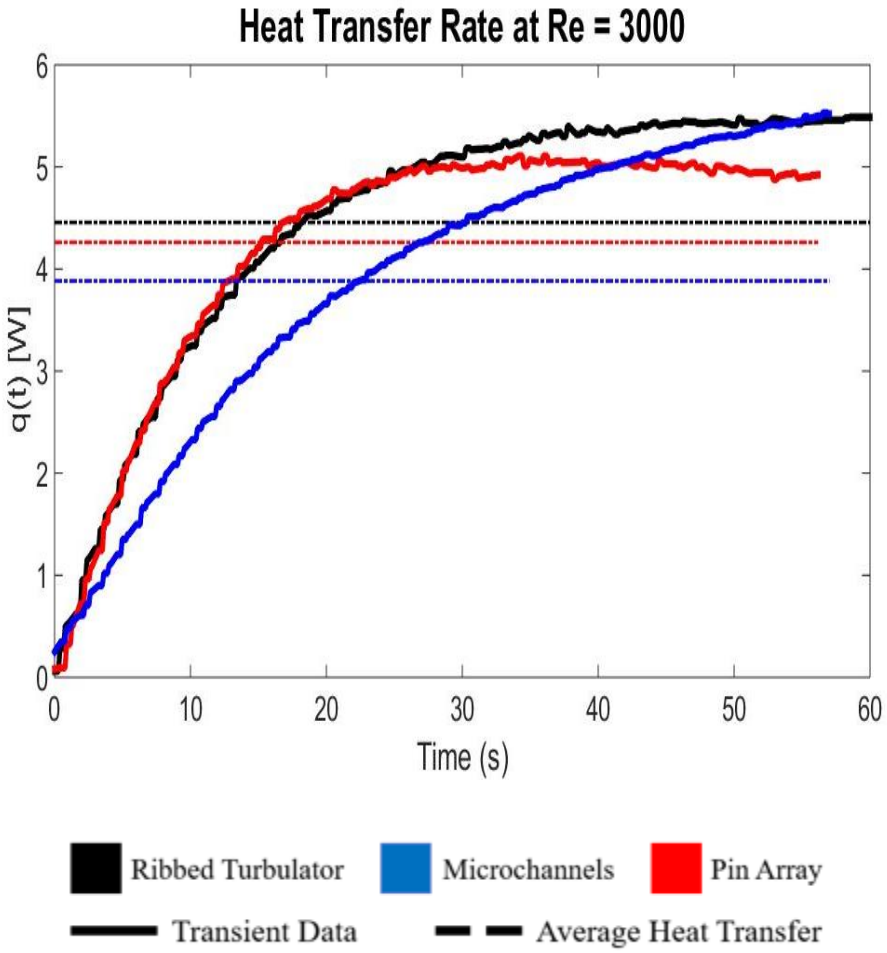

Figure 19: Bulk flow analysis heat transfer rate at Re = 3000 for each cooling configuration

Despite showing better heat transfer across most cases in the bulk flow analysis, a distinct disadvantage of both the ribbed turbulator and pin-fin array configurations is the lack of heat being displaced to the trailing edge of the test article. This is shown through comparison of the transient infrared images taken at the initial and final time step for each test shown in Figures 20-22 below. Within these plots, the trailing edge of the test article is located at the maximum value in the spanwise direction of the plot. The inlet of the test piece corresponds to points occurring at the maximum streamwise value within the image. Within the progression of images shown in Figure 20, the ribbed turbulator configuration displays minimal convective coverage of the trailing edge at lower Reynolds numbers flows. At higher Reynolds number, the trailing edge exhibits a rise in temperature near the inlet region. However, minimal change in temperature is shown at the trailing and over the 60-90 pixel range in the spanwise direction near the outlet of the test article for the transient time period.

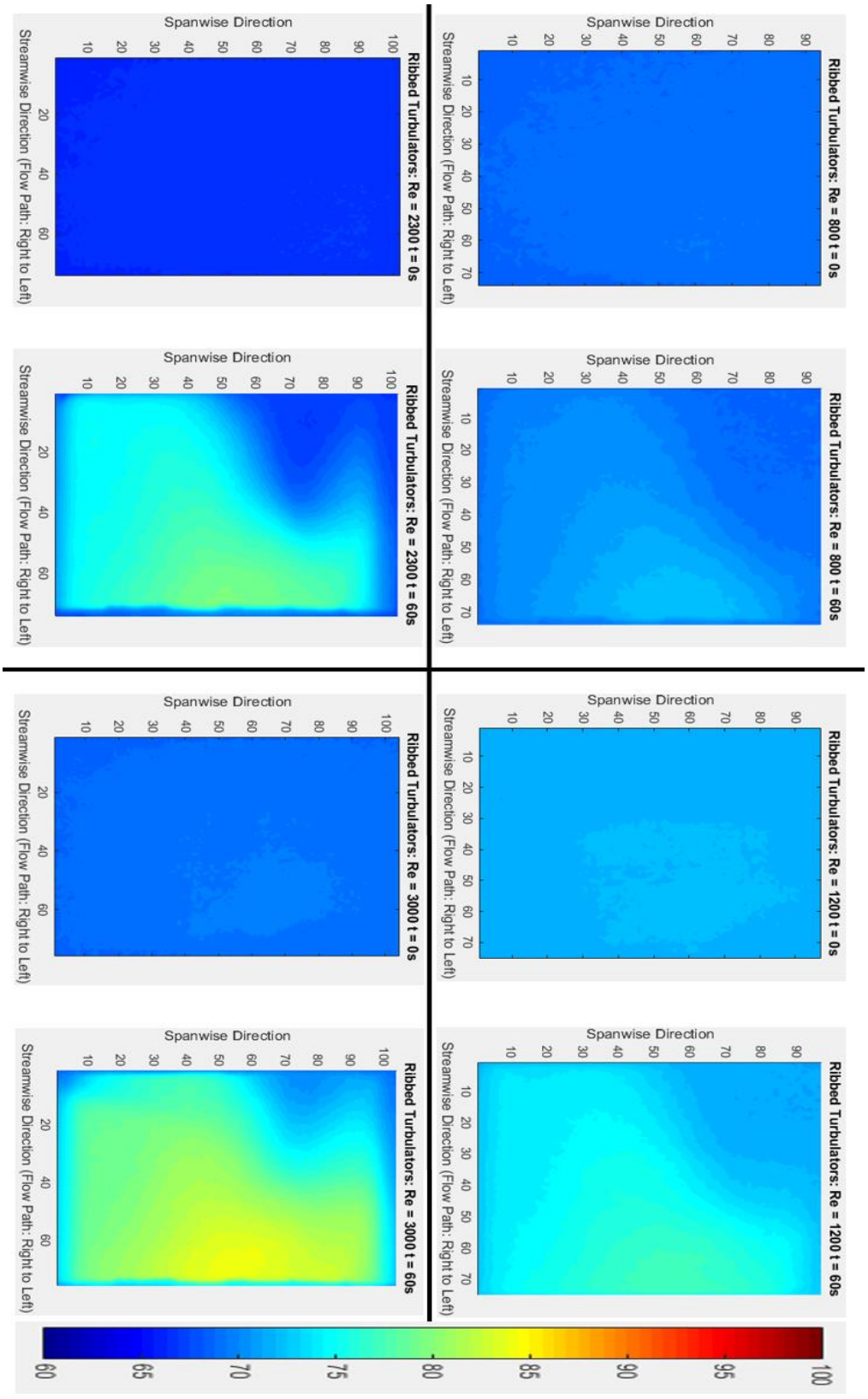

Figure 20: First & last temperature profiles for each Ribbed Turbulator test

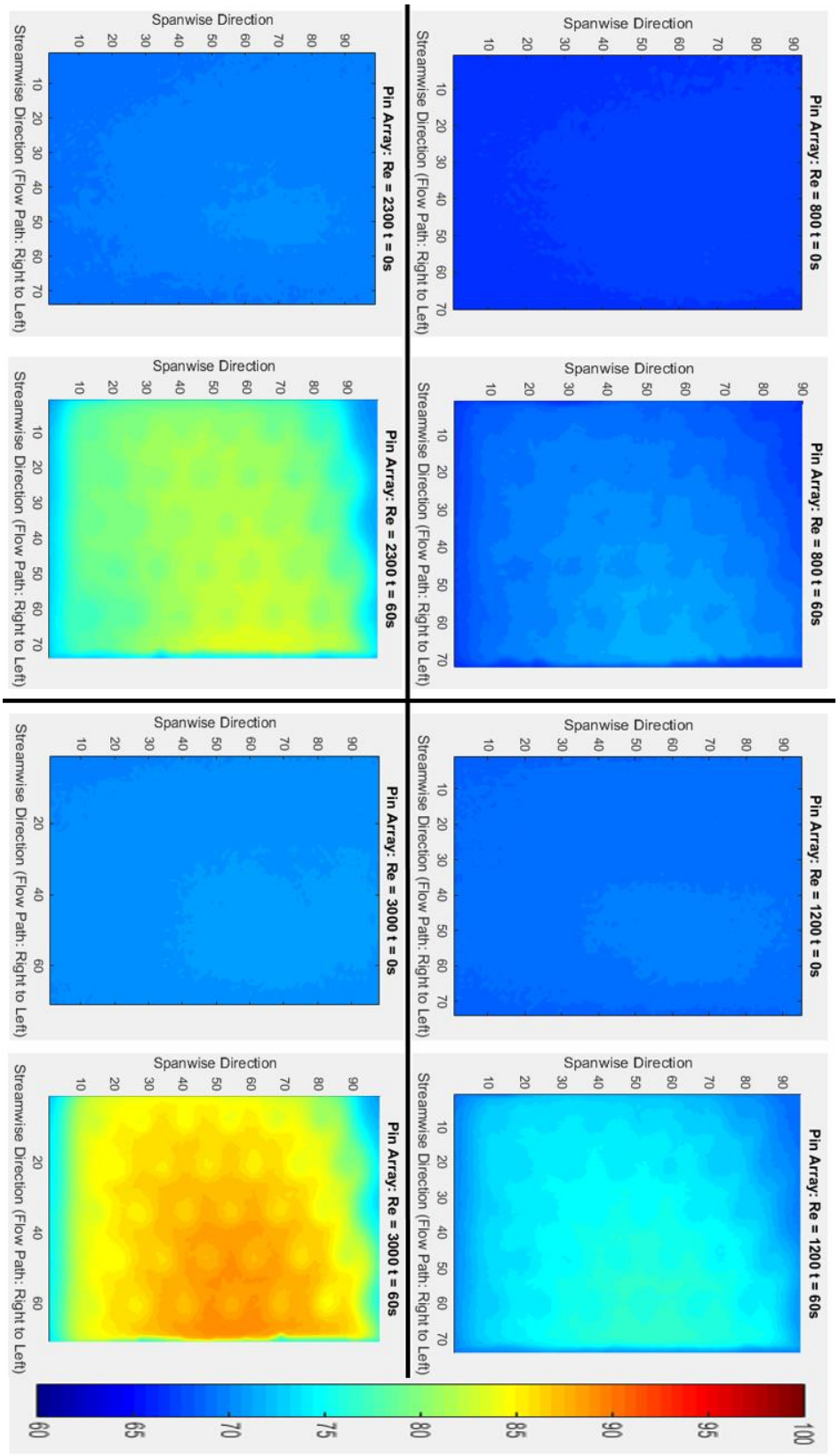

Figure 21: First and last temperature profiles for each Pin-Fin Array test

From observing Figure 21, it is apparent that the pin-fin configuration displays significant changes in temperature across all tests for the transient time period when compared to the ribbed turbulator and microchannel configurations. Because of the net change in temperature displayed across the majority of the test article, it would appear that the pin-fin array provides the most effective method for heat transfer for the majority of the region. However, this does not hold true for the trailing edge. As shown by final time step images shown in Figure 21, the pin-fin array exhibits minimal coverage of the trailing edge region near the outlet of the test article.

Therefore, it cannot be said that this configuration it best suited to provide adequate heat transfer augmentation at the true trailing edge of the test article geometry.

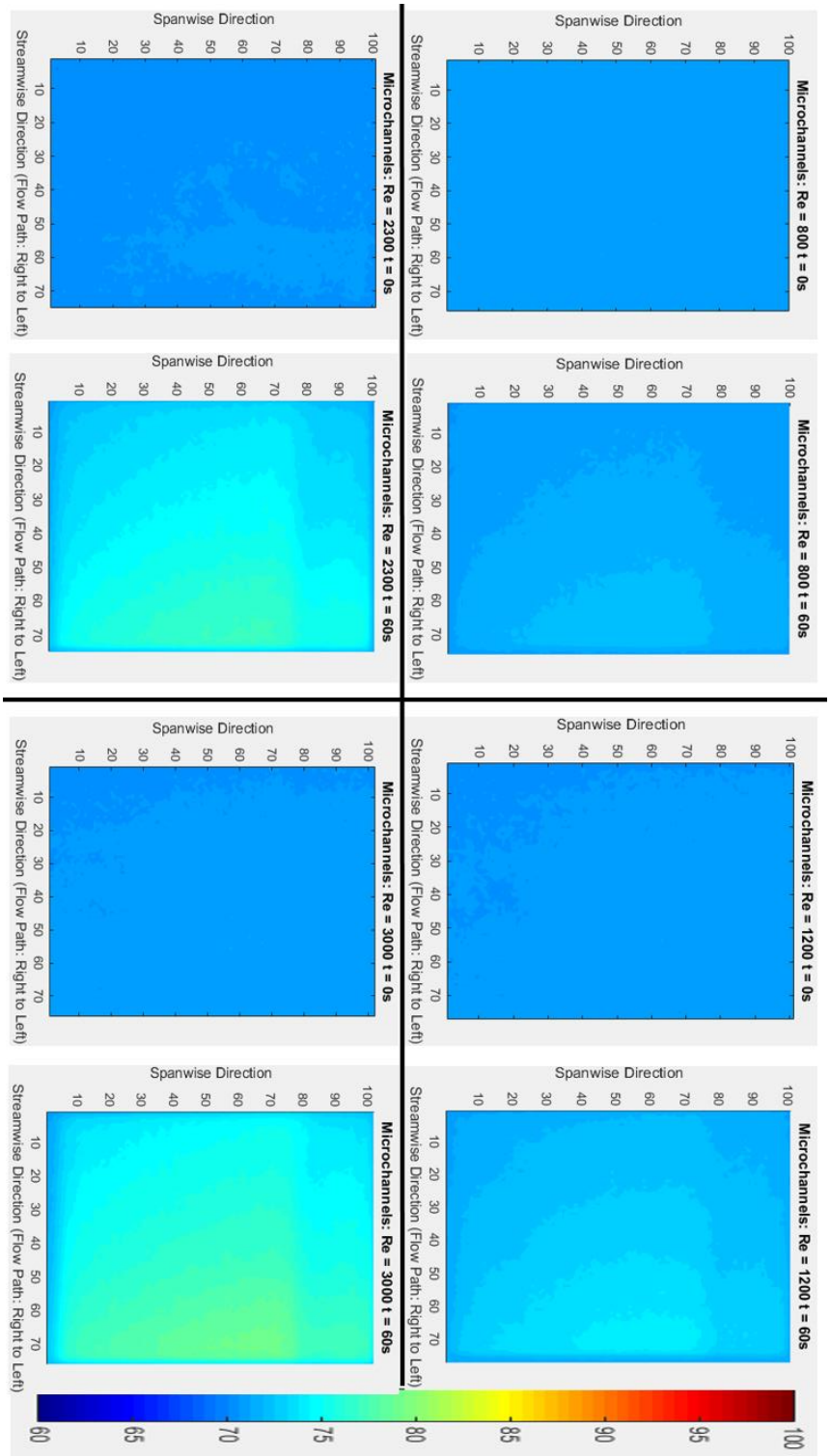

Figure 22: First and last temperature profiles for each Microchannel test

As shown within Figures 20-22 below, only the microchannel configuration succeeds in displaying convective heat transfer along the full span of the trailing edge. At low Reynolds number flows within this geometry, there is a lag in net temperature change across the trailing edge. As Reynolds number increases, addition fluid is carried through the test article and increased heating along the length of the trailing edge is shown. Although the temperature change shown is not as large as those exhibited in the ribbed turbulator and pin-fin array configurations, these images convey a competitive advantage in the use of microchannels at the true trailing edge. From Figures 20-22, it is reasonable to believe that combining pin-fin arrays and microchannels within a trailing edge configuration could provide additional benefit to heat transfer augmentation. Within practical application of the cooling geometries, this lack of coverage on the part of the ribbed turbulator and the pin-fin array could create an unwanted hotspot at the trailing edge near the tip. As a result, degradation of the trailing edge at the uncooled spot would lead to efficiency losses in the turbine and additional cost to component life and result in additional expenditure to replace the damaged vane.

4.2 3D Inverse Transient Solution

Internal heat transfer coefficients for each model were found via iterating upon the heat transfer models until convergence between surface average heat transfer coefficients was found between successive iterations of the model. Table 5 below displays the converged values output by the heat transfer models. Pertinent values within the table include the predicted average surface temperature (Column 5 of Table 5) and predicted surface average heat transfer coefficient of the internal wall surface (Column 6 of Table 5). For each of these values, area averages were taken across the respective surfaces for which these values correlate. Within each of these models, coolant temperature was specified as 300K. Although coolant temperature varied with time during a test, the use of time varying temperature within the model produced significant divergence within the present study. Therefore, a constant value across tests was specified to reduce bias between tests. Exploration of the cause of divergence, and subsequently the successful implementation of time varying fluid temperature, is currently being explored for improvement of future heat transfer models of the current system. Wall temperature is not specified within the model as this value varies within internal heat transfer coefficient.

Table 5: Convergence criterion for 3D inverse heat conduction models

Model	Reynolds Number	Base Size (mm)	Avg Surface Temp - IR (K)	Average Surface Temp - Predicted (K)	Surface Average HTC - Predicted (W/m^2-K)	% Difference Temp	% Difference HTC	# Cells
Pin Array	800	0.400	293.78	293.09	**8.312**	0.24	1.80	106919
	800	0.300	293.78	293.85	**8.163**	0.02		206597
	1200	0.300	294.77	295.14	**36.688**	0.13	2.93	206597
	1200	0.200	294.77	295.14	**37.779**	0.13		633797
	2300	0.300	296.84	297.05	**61.083**	0.07	3.58	206597
	2300	0.175	296.84	297.05	**63.308**	0.07		953178
	3000	0.300	298.49	DNC	DNC	DNC	-	206597
	3000	0.200	298.49	DNC	DNC	DNC		633797
Microchannel	800	0.400	295.00	295.04	**2.147**	0.01	0.23	1143397
	800	0.300	295.00	295.04	**2.153**	0.01		2504566
	1200	0.400	295.16	295.18	**3.650**	0.01	0.45	1143397
	1200	0.300	295.16	295.18	**3.666**	0.01		2504566
	2300	0.400	295.33	295.39	**5.360**	0.02	0.66	1143397
	2300	0.300	295.33	295.39	**5.396**	0.02		2504566
	3000	0.400	295.88	295.90	**8.007**	0.01	4.93	1143397
	3000	0.300	295.88	295.95	**8.411**	0.02		2504566
Ribbed Turbulator	800	0.400	294.17	294.25	**4.611**	0.03	3.41	2610933
	800	0.300	294.17	294.28	**4.771**	0.04		5925126
	1200	0.500	295.49	294.31	**11.001**	0.40	2.79	1560157
	1200	0.300	295.49	295.59	**10.698**	0.03		5925126
	2300	0.500	293.86	293.99	**24.113**	0.04	1.45	1560157
	2300	0.400	293.86	293.96	**23.766**	0.03		2610933
	3000	0.400	296.64	DNC	DNC	DNC	-	2610933
	3000	0.300	296.64	DNC	DNC	DNC		5925126

As indicated by the table, all heat transfer coefficients converged to values within 5% of same model simulations. In addition, the average surface temperature output by the model converged with that of the measured case by less than 1%. Within simulations, two test cases did not converge: the pin array configuration at Re = 3000 & the ribbed turbulator configuration at Re = 3000. Within successive iterations of the model, divergence was inherent despite increased mesh size and time step refine, in addition to the implementation of relaxation factors in the calculation of the temperature ratio per Equation (4). It would appear that the relative complexity of the models, large temperature change over the transient, and relative variation within temperature profile across the measured surface may be factors within the divergence of these cases. Future model iterations will be conducted across shorter time intervals within the transient to further explore this divergence.

Additional analysis was performed to evaluate the correlation between the heat transfer rate calculated using bulk flow analysis and the heat transfer rate found using outputs of the heat transfer models. As shown in Table 6 below, heat transfer rates found within each method did not achieve convergence.

Table 6: Correlation between Bulk Flow Analysis and Thermal Interia HTC method heat transfer rate

Model	Re	Heat Transfer Rate - Bulk Flow [W]	Heat Transfer Rate - Model [W]	% Difference
Pin Array	800	0.82	0.17	131.2
	1200	1.02	0.64	45.9
	2300	3.44	0.56	143.6
	3000	4.99	-	-
Microchannels	800	0.50	0.04	173.2
	1200	0.85	0.06	172.6
	2300	2.81	0.08	188.4
	3000	4.42	0.11	190.3
Ribbed Turbulator	800	0.63	0.09	149.9
	1200	0.66	0.16	123.2
	2300	4.80	0.45	165.8
	3000	5.34	-	-

Further evaluation of the system will be required to determine sources of deviation between the two methods of calculation.

For the converged cases, surface average Nusselt number ($\overline{Nu}$) was calculated for each test article per Equation (7):

$$\overline{Nu} = \frac{\bar{h} D_h}{k} \tag{7}$$

where $\bar{h}$ corresponds to the average heat transfer coefficient across the internal wall of the test article. As shown by Figure (23) below, the pin-fin array provides to greatest cooling benefit over the entire spectrum of mass flows tested, followed by the ribbed turbulators.

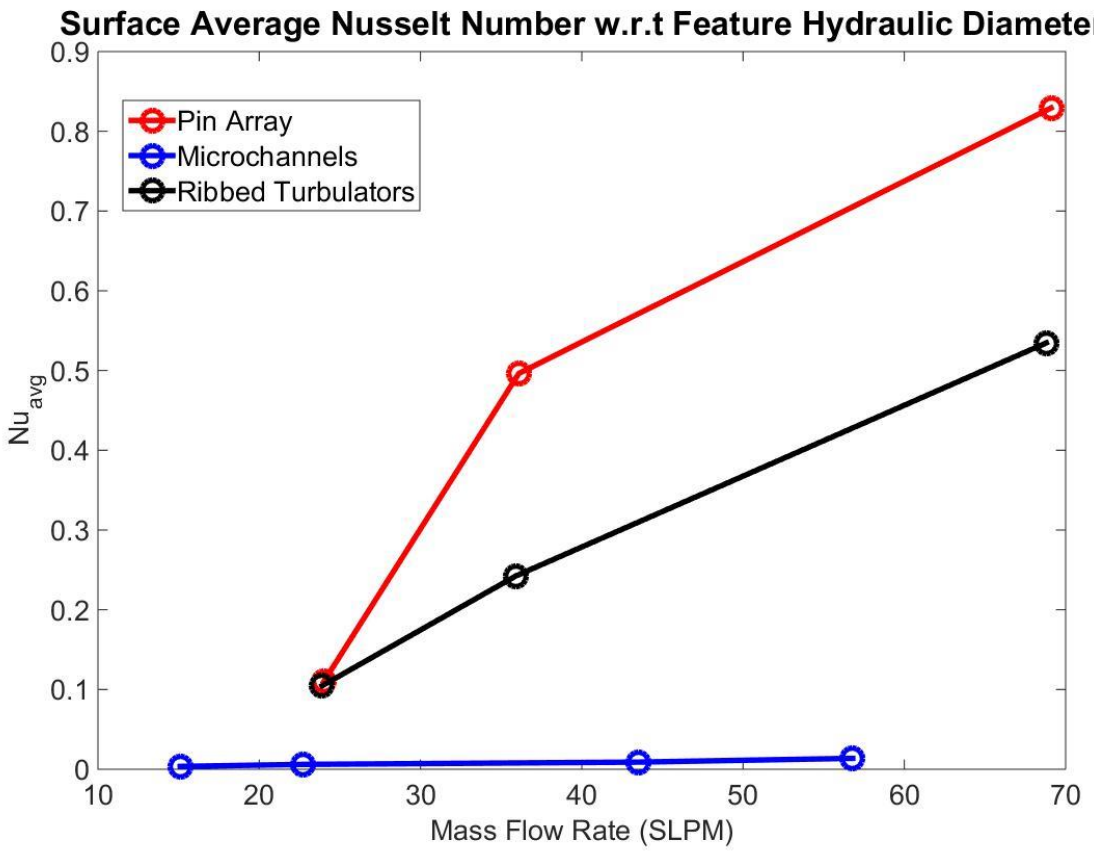

Figure 23: Surface average Nusselt Number vs. Mass flow rate

As shown by Figure (23), when compared directly, microchannels appear to perform very poorly when compared to the pin-fin array and ribbed turbulators. However, this small Nusselt number value is not unreasonable for the microchannels as the combined hydraulic diameter of the microchannels is very small with respect both the pin-fin cooling channel and ribbed turbulator cooling channel. In an attempt to create a fair comparison between the three configurations, Figure (24) applies a correction factor to the surface average Nusselt number to account for bias in the total flow area between test articles. As shown within the comparative analysis of Figures 20-22, minimal flow area and high pressure drop across the microchannel configuration resulted in smaller amounts of convective fluid flow to be passed through the microchannel test article, when compared to the pin-fin array and ribbed turbulator test articles, within the 60 second transient test. As a larger number of microchannels within the test article would allow for a reduced pressure drop across the test article and an increase in permitted mass flow throughout the transient test, it is reasonable to assume that a fairer comparison could be

made across cooling configurations if bias in total flow area was eliminated as a variable within testing.

Equation (7) below displays the correction factor utilized to eliminate total flow area bias and adjusted Nusselt number values are displayed within Figure (24):

$$\frac{A_{max}}{A_{cs,feature}} = \frac{Pin\ C.S.\ Area}{C.S.\ Area\ of\ Test\ Article\ Channel} \tag{8}$$

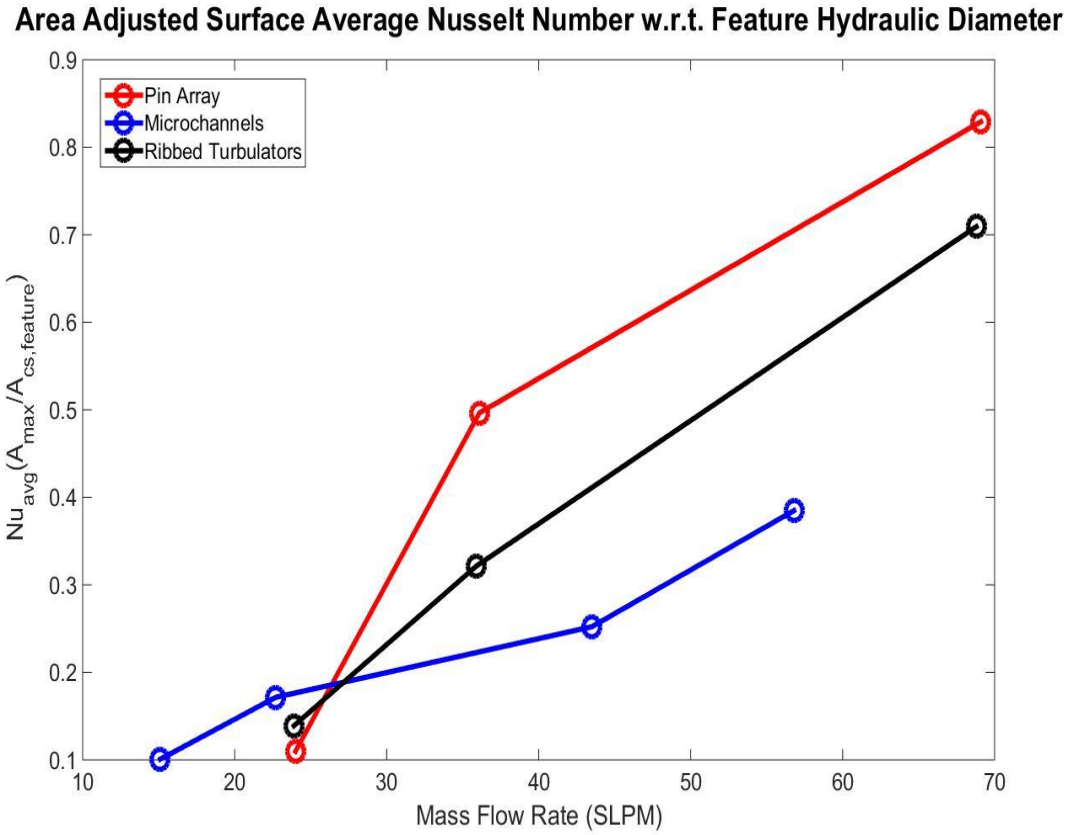

Figure 24: Surface average Nusselt number for various mass flow rates corrected for channel flow area.

Within this correction factor, the surface average Nusselt number of each cooling configuration is multiplied by the ratio of the maximum flow area out of all three configurations and the flow area of the configuration in question. Because the pin cross-sectional flow area is the largest of the three, it is defined as A_{max} and the applied ratio results in no change to the Nusselt number of the pin-fin array. The ribbed turbulator Nusselt number value is adjusted by a

factor of 1.33, resulting in negligible change at higher mass flows. However, at a mass flow rate of 25 [SLPM], it appears that the ribbed turbulator has a slight advantage when compared to the pin-fin array. The microchannel configuration is adjusted by a factor of 28.13 when adjusted by this ratio. This adjustment theoretically acts to simulate the addition of approximately 28 microchannels to the array. Although this proves to have minimal significance at higher mass flow rates, the trend displayed in Figure (24) suggests that a denser array of microchannels would exhibit a greater cooling benefit than both the pin-fin array and ribbed turbulators as mass flow decreases. Further testing will be required to ensure the tangibility of these results.

4.3 Pressure Drop

Within an internal cooling channel is important that pressure drop is low across the channel to ensure maximum mass flow efficiency of the coolant. Pressure drop was measured as the pressure difference between pressure measurements output by the mass flow meter just before the start of the test, and at the 30 second point during the transient. Table 6 below displays the pressure drop across the test article.

Table 7: Measured pressure drop across the test article

Pressure Drop Across the Test Article [psi]			
Reynolds Number	Microchannel	Pin Fin Array	Ribbed Turbulator
800	0.76	0.01	0.17
1200	1.3	0.36	0.41
2300	2.84	1.23	1.31
3000	3.65	1.86	2.11

Across all tests, microchannels displayed the worst mass flow efficiency of all cooling configurations tested. These results appear reasonable from Equation (10) as derived from Equation (9) per [24] as the hydraulic diameter of the microchannels configuration is much lower than the channel length:

$$f_{Dh} = \frac{\Delta p}{2\rho {u_m}^2} \times \frac{D_h}{L_{channel}} \tag{9}$$

$$\Delta p = 2\rho f_{Dh} {u_m}^2 \frac{L_{channel}}{D_h} \tag{10}$$

At comparable mass flows, pin-fin arrays and ribbed turbulators displayed similar mass flow efficiency.

Chapter 5: Conclusions

Microchannels, ribbed turbulators, and pin arrays were comparatively analyzed for heat transfer effectiveness within a trailing edge configuration. Internal heat transfer coefficients of each test article were measured across a range of Reynolds numbers using the Thermal Inertia Heat Transfer Coefficient technique. Secondary analyses performed analyzed pressure drop and bulk flow across the test article. At higher values of Reynold's number, microchannel cooling shows potential for higher heat transfer rates at steady state. This is indicated within the bulk flow analysis through the increasing heat transfer rate displayed by microchannels across all tests. Microchannel cooling also exhibits potential for high surface heat transfer rates given a denser array of microchannels. Application of microchannel cooling may be better suited for trailing edge ejection as decreased channel length will result in lower pressure difference across the channel. This would also allow for increased cooling to reach the true trailing edge in practical application. As a final note, microchannel cooling displays cooling benefit at lower mass flow rates when factoring for the difference in total area of the cooling channels.

For the current system, additional testing at the present mass flow values more turbulent flow regimes will be conducted for the current test articles. Re-design of sealing mechanism within the current test apparatus will also be explored to allow for higher mass flows to be explored. Future tests will also be conducted on the basis of constrained pressure drop rather than similitude about a Reynolds number. This change has been deemed necessary as it emulates practical turbine design. Therefore, evaluation of heat removal at fixed pressure ratios will be used for future testing. This study provides a baseline analysis upon which future analysis of microchannel implementation into a nozzle guide vane configuration. Computational modeling of additional microchannel cooling configurations will be used to determine optimal use of microchannels within the trailing edge region. One potential study to be explored would be comparison of pedestals, microchannel arrays, and straight slots for use in trailing edge ejection. Another study could take into account the heat transfer benefit of trailing edge cooling at the true trailing edge and combine it with an optimal pin configuration in the forward trailing edge region. Conjugate heat transfer model analysis will be used to analyze each cooling configuration. Experimental evaluation of optimal designs produced within these studies could

be tested at engine relevant conditions. Nusselt number analysis varying array density and distance from the cooled surface can also be performed.

References

[1] M. Ohadi, K. Choo, S. Dessiatoun, E. Cetegen, "Next Generation Microchannel Heat Exchangers," SpringerBriefs in Thermal Engineering and Applied Science, DOI: 10.1007/978-1-4614-0779-9_1,© The Authors 2013.

[2] How Gas Turbine Power Plants Work. (n.d.). Retrieved April 02, 2017, from https://energy.gov/fe/how-gas-turbine-power-plants-work

[3] University of Virginia Wadley Research Group, (2013), "High Temperature Coatings". Retrieved from: http://www.virginia.edu/ms/research/wadley/high-temp.html.

[4] J. C. Han, S. Dutta, and S.V. Ekkad, "Gas Turbine Heat Transfer and Cooling Technology, Second Edition." New York, New York: Taylor and Francis, 2000.

[5] K. M. Kim, H. Lee, B.S. Kim, S. Shin, D.H. Lee, & H.H. Cho, "Optimal design of angled rib turbulators in a cooling channel," *Journal of Heat and Mass Transfer*: vol. 45, no. 12, pp. 1617-1625, 2009

[6] S. Gupta, A. Chaube, & P. Verma. "Review on Heat Transfer Augmentation Techniques: Application in Gas Turbine Blade Internal Cooling. *Journal of Engineering Science & Technology Review, 5,* 1, 2012.

[7] J.C. Han, Y.M. Zhang, C.P. Lee, "Augmented heat transfer in square channels with parallel, crossed, and V-shaped angled ribs," ASME Journal of Heat Transfer, vol. 113, pp. 590-596, 1991.

[8] S.C. Lau, Y.S. Kim, J.C. Han, "Effects of fin configuration and entrance length on local endwall heat/mass transfer in a pin fin channel. ASME Paper 85-WA/HT-62.

[9] B. A. Brigham and G. J. VanFossen, "Length to Diameter Ratio and Row Number Effects in Short Pin Fin Heat Transfer," J. Eng. Gas Turbines Power, vol. 106, no. 1, pp.

241–245, 1984.

[10] R. J. Simoneau and G. J. VanFossen, “Effect of location in an array on heat transfer to a short cylinder in crossflow,” Journal of Heat Transfer, vol. 106, no. 1, pp. 42– 8, 1984.

[11] G. J. VanFossen, “Heat Transfer Coefficients for Staggered Arrays of Short Pin Fins,” *ASME Paper No. 81 -GT-75,* 1981.

[12] D. E. Metzger, W. B. Shepard, and S. W. Haley, “Row Resolved Heat Transfer Variations in Pin-Fin Arrays Including Effects of Non-Uniform Arrays and Flow Convergence,” *ASME Paper No. 86-GT-132,* 1986.

[13] M. E. Lyall, A. A. Thrift, K. A. Thole, and A. Kohli, “Heat transfer from low aspect ratio pin fins,” *Journal of Turbomachinery,* vol. 133, no. 1, 2011.

[14] S. A. Lawson, A. A. Thrift, K. A. Thole, and A. Kohli, “Heat transfer from Multiple Row Arrays of Low Aspect Ratio Pin Fins,” *Int. J. Heat Mass Transfer,* vol. 54, no. 17–18, pp. 4099–4109, 2011.

[15] Aziz Belmiloudi. “Heat Transfer - Theoretical Analysis, Experimental Investigations and Industrial Systems,” InTech (Open access Publisher) Vienna, Chapter 5 – Microchannel Heat Transfer, 2011.

[16] S.A. Weaver, M.D. Barringer, & K.A. Thole, “Microchannels with manufacturing roughness levels.” *Journal of Turbomachinery,* vol. 133, no. 4. pp. 041014 1-8, 2011.

[17] J.C. Snyder, C.K. Stimpson, K.A. Thole, & D.J. Mongillo, “Build direction effects on microchannel tolerance and surface roughness.” *Journal of Mechanical Design*. vol. 137, no. 11, pp. 111411-1-8, 2015.

[18] K. Kiersch & K. Thole, “Heat transfer and pressure loss measurements in additively

manufactured wavy microchannels", *Journal of Turbomachinery*. vol. 139, no. 1, pp. 11007-1-9, 2017.

[19] J. Zhang, P.T. Lin, & Y. Jaluria, "Design and optimization of multiple microchannel heat transfer systems." Journal of Thermal Science and Engineering Applications, vol. 6, pp. 011004-1-10, 2014.

[20] Single-phase convective heat transfer in microchannels: a review of experimental results, Gian Luca Morini, *International Journal of Thermal Sciences*, Vol. 43, Iss. 7, pp. 631-651, 2004

[21] G.L. Morini, & Y. Yang, "Guidelines for the Determination of Single-Phase Forced Convection Coefficients in Microchannels". *Journal of Heat Transfer*, vol. 135, no. 10, pp. 101004-1-10, 2013

[22] R.S. Bunker, T.G. Wetzel, & D.L. Rigby, "Heat transfer in a complex trailing edge passage for a high pressure turbine blade – part 1: experimental measurements." *IGTI Proceedings*, GT-2002-30212, pp. 1-7, 2002.

[23] N.V. Nirmalan, R.S. Bunker, & C.R. Hedlund, "The Measurement of Full-Surface Internal Heat Transfer Coefficients for Turbine Airfoils Using a Nondestructive Thermal Inertia Technique." *Journal of Turbomachinery*, vol. 125, pp. 83-89, 2003.

[24] Bergman, T. L., Bergman, T. L., Lavine, A., Incropera, F. P., & DeWitt, D. P. (2011). Introduction to heat transfer.

[25] Ohio Supercomputer Center. 1987. Ohio Supercomputer Center. Columbus OH: Ohio Supercomputer Center. http://osc.edu/ark:/19495/f5s1ph73.

Appendix A: MATLAB Codes

A1: Mass Flow Rate Calculations

```
% Mass flow rate calculations
%   All calculations are based in the metric unit system
clear all; close all; clc;
%Standard Air Properties
%   Air temp is roughly 100F = 310.928K
airTemp = 310.928;  %K
airPressure_in = 1; %atm
%   Properties to be interpolated from Table A4 from Introduction to Heat
%   Transfer 6th Edition - Incropera
airDensity_300 = 1161.4; %[g/m^3]
airDensity_350 = 995.0; %[g/m^3]
airDensity = airDensity_300 + (((airDensity_350)-(airDensity_300))*(airTemp -
300))/(50);
airViscosity_mu_300 = 184.6*10^-7;  %Ns/m^2
airViscosity_mu_350 = 208.2*10^-7;  %Ns/m^2
airViscosity_mu = airViscosity_mu_300 + (((airViscosity_mu_350)-
(airViscosity_mu_300))*(airTemp - 300))/(50);

%Set up range of Reynold's numbers to determine range of mass flow rate
Re_Dh = [800,1200,2300,3000];

% Microchannels
nMicrohannels = 35;
microchannelWidth = 0.375*10^-3;  %m
microchannelHeight = 0.75*10^-3;  %m
microchannelA_cs = microchannelWidth*microchannelHeight;    %m^2
microchannelPerimeter = 2*microchannelWidth + 2*microchannelHeight; %m
microchannelD_h = ((4*microchannelA_cs)/microchannelPerimeter);
microchannelRhoU = (Re_Dh.*airViscosity_mu)./microchannelD_h;   %kg/(m^2*s)
microchannelM_dot = microchannelRhoU.*microchannelA_cs; %kg/s
microchannelTotalM_dot = nMicrohannels.*microchannelM_dot.*1000; %[g/s] 35 is
the number of microchannels

microchannelSLPM = (microchannelTotalM_dot./1000).*60000./1.184;

maxMicroM_dot = max(microchannelTotalM_dot) %g/s
minMicroM_dot = min(microchannelTotalM_dot) %g/s
maxMicroSLPM = max(microchannelSLPM) %L/min
minMicroSLPM = min(microchannelSLPM) %L/min

% Pin Arrays
%   Perimeters and Areas measured within SolidWorks
pinPerimeter = 0.124968;   %in
pinArea_cs = 0.010907;     %in
pinD_h = (4*pinArea_cs)/pinPerimeter;
pinRhoU = (Re_Dh.*airViscosity_mu)./pinD_h; %kg/(m^2*s)
pinM_dot = pinRhoU.*pinArea_cs*1000; %g/s

maxPinM_dot = max(pinM_dot) %g/s
minPinM_dot = min(pinM_dot) %g/s
```

```
pinSLPM = (pinM_dot./1000).*60000./1.184;
maxPinSLPM = max(pinSLPM) %L/min
minPinSLPM = min(pinSLPM) %L/min

% Ribbed Turbulator
%   Perimeters and Areas measured within SolidWorks
ribPerimeter = 0.12446;   %m
ribThin_Height = 0.001; %m
ribThin_Length = 0.01495722376; %m
ribBase_Height = 0.00811697512; %m
ribBase_Length = 0.04250105869; %m
ribArea_cs =
(ribThin_Height*ribThin_Length)+(0.5*(ribThin_Height+ribBase_Height)*ribBase_
Length);    %m
ribD_h = (4*ribArea_cs)/ribPerimeter;
ribRhoU = (Re_Dh.*airViscosity_mu)./ribD_h; %kg/(m^2*s)
ribM_dot = ribRhoU.*ribArea_cs*1000; %g/s

maxRibM_dot = max(ribM_dot) %g/s
minRibM_dot = min(ribM_dot) %g/s

ribSLPM = (ribM_dot./1000).*60000./1.184;
maxRibSLPM = max(ribSLPM) %L/min
minRibSLPM = min(ribSLPM) %L/min
```

A2: Bulk Flow Analysis Calculations

```
%Read in all of the files
% Pin800 = dlmread('PinArray800_thermocouple.csv','\t',1,0);
% Pin1200 = dlmread('PinArray1200_thermocouple.csv','\t',1,0);
% Pin2300 = dlmread('PinArray2300_thermocouple.csv','\t',1,0);
% Pin3000 = dlmread('PinArray3000_thermocouple.csv','\t',1,0);
% MC800 = dlmread('Microchannel800_thermocouple.csv','\t',1,0);
% MC1200 = dlmread('Microchannel1200_thermocouple.csv','\t',1,0);
% MC2300 = dlmread('Microchannel2300_thermocouple.csv','\t',1,0);
% MC3000 = dlmread('Microchannel3000_thermocouple.csv','\t',1,0);
% RT800 = dlmread('RibbedTurbulator800_thermocouple.csv','\t',1,0);
% RT1200 = dlmread('RibbedTurbulator1200_thermocouple.csv','\t',1,0);
% RT2300 = dlmread('RibbedTurbulator2300_thermocouple.csv','\t',1,0);
% RT3000 = dlmread('RibbedTurbulator3000_thermocouple.csv','\t',1,0);

%Mass Flow in kg/s for each test
m_dotRT800 = 0.4723/1000;
m_dotRT1200 = 0.7085/1000;
m_dotRT2300 = 1.3250/1000;
m_dotRT3000 = 1.7713/1000;

m_dotMC800 = 0.2989/1000;
m_dotMC1200 = 0.4483/1000;
m_dotMC2300 = 0.8592/1000;
m_dotMC3000 = 1.1208/1000;

m_dotPA800 = 0.4743/1000;
m_dotPA1200 = 0.7114/1000;
m_dotPA2300 = 1.3635/1000;
m_dotPA3000 = 1.7785/1000;
%Pin Values
pa800T1 = (Pin800(:,1)-32)*(5/9)+273.15;
pa800T2 = (Pin800(:,2)-32)*(5/9)+273.15;
pa800T3 = (Pin800(:,3)-32)*(5/9)+273.15;
pa800T4 = (Pin800(:,4)-32)*(5/9)+273.15;
pa800time = Pin800(:,5);

pa1200T1 = (Pin1200(:,1)-32)*(5/9)+273.15;
pa1200T2 = (Pin1200(:,2)-32)*(5/9)+273.15;
pa1200T3 = (Pin1200(:,3)-32)*(5/9)+273.15;
pa1200T4 = (Pin1200(:,4)-32)*(5/9)+273.15;
pa1200time = Pin1200(:,5);

pa2300T1 = (Pin2300(:,1)-32)*(5/9)+273.15;
pa2300T2 = (Pin2300(:,2)-32)*(5/9)+273.15;
pa2300T3 = (Pin2300(:,3)-32)*(5/9)+273.15;
pa2300T4 = (Pin2300(:,4)-32)*(5/9)+273.15;
pa2300time = Pin2300(:,5);

pa3000T1 = (Pin3000(:,1)-32)*(5/9)+273.15;
pa3000T2 = (Pin3000(:,2)-32)*(5/9)+273.15;
pa3000T3 = (Pin3000(:,3)-32)*(5/9)+273.15;
pa3000T4 = (Pin3000(:,4)-32)*(5/9)+273.15;
pa3000time = Pin3000(:,5);
```

```
%Microchannel values
mc800T1 = (MC800(:,1)-32)*(5/9)+273.15;
mc800T2 = (MC800(:,2)-32)*(5/9)+273.15;
mc800T3 = (MC800(:,3)-32)*(5/9)+273.15;
mc800T4 = (MC800(:,4)-32)*(5/9)+273.15;
mc800time = MC800(:,5);

mc1200T1 = (MC1200(:,1)-32)*(5/9)+273.15;
mc1200T2 = (MC1200(:,2)-32)*(5/9)+273.15;
mc1200T3 = (MC1200(:,3)-32)*(5/9)+273.15;
mc1200T4 = (MC1200(:,4)-32)*(5/9)+273.15;
mc1200time = MC1200(:,5);

mc2300T1 = (MC2300(:,1)-32)*(5/9)+273.15;
mc2300T2 = (MC2300(:,2)-32)*(5/9)+273.15;
mc2300T3 = (MC2300(:,3)-32)*(5/9)+273.15;
mc2300T4 = (MC2300(:,4)-32)*(5/9)+273.15;
mc2300time = MC2300(:,5);

mc3000T1 = (MC3000(:,1)-32)*(5/9)+273.15;
mc3000T2 = (MC3000(:,2)-32)*(5/9)+273.15;
mc3000T3 = (MC3000(:,3)-32)*(5/9)+273.15;
mc3000T4 = (MC3000(:,4)-32)*(5/9)+273.15;
mc3000time = MC3000(:,5);

%Ribbed Turbulator values
rt800T1 = (RT800(:,1)-32)*(5/9)+273.15;
rt800T2 = (RT800(:,2)-32)*(5/9)+273.15;
rt800T3 = (RT800(:,3)-32)*(5/9)+273.15;
rt800T4 = (RT800(:,4)-32)*(5/9)+273.15;
rt800time = RT800(:,5);

rt1200T1 = (RT1200(:,1)-32)*(5/9)+273.15;
rt1200T2 = (RT1200(:,2)-32)*(5/9)+273.15;
rt1200T3 = (RT1200(:,3)-32)*(5/9)+273.15;
rt1200T4 = (RT1200(:,4)-32)*(5/9)+273.15;
rt1200time = RT1200(:,5);

rt2300T1 = (RT2300(:,1)-32)*(5/9)+273.15;
rt2300T2 = (RT2300(:,2)-32)*(5/9)+273.15;
rt2300T3 = (RT2300(:,3)-32)*(5/9)+273.15;
rt2300T4 = (RT2300(:,4)-32)*(5/9)+273.15;
rt2300time = RT2300(:,5);

rt3000T1 = (RT3000(:,1)-32)*(5/9)+273.15;
rt3000T2 = (RT3000(:,2)-32)*(5/9)+273.15;
rt3000T3 = (RT3000(:,3)-32)*(5/9)+273.15;
rt3000T4 = (RT3000(:,4)-32)*(5/9)+273.15;
rt3000time = RT3000(:,5);

%Method 1

%RT800
Tin_rt800 = (rt800T1+rt800T2)/2; %K
```

```
Tout_rt800 = (rt800T3+rt800T4)/2; %K
Tavg_rt800 = (Tin_rt800+Tout_rt800)/2;
cp_rt800 = 4184*(0.2269807*exp((0.000097247*(Tavg_rt800*(9/5))))); %J/kg-K
q_rt800 = m_dotRT800.*cp_rt800.*(Tin_rt800-Tout_rt800); %W

%RT1200
Tin_rt1200 = (rt1200T1+rt1200T2)/2; %K
Tout_rt1200 = (rt1200T3+rt1200T4)/2; %K
Tavg_rt1200 = (Tin_rt1200+Tout_rt1200)/2;
cp_rt1200 = 4184*(0.2269807*exp((0.000097247*(Tavg_rt1200*(9/5))))); %J/kg-K
q_rt1200 = m_dotRT1200.*cp_rt1200.*(Tin_rt1200-Tout_rt1200); %W

%RT2300
Tin_rt2300 = (rt2300T1+rt2300T2)/2; %K
Tout_rt2300 = (rt2300T3+rt2300T4)/2; %K
Tavg_rt2300 = (Tin_rt2300+Tout_rt2300)/2;
cp_rt2300 = 4184*(0.2269807*exp((0.000097247*(Tavg_rt2300*(9/5))))); %J/kg-K
q_rt2300 = m_dotRT2300.*cp_rt2300.*(Tin_rt2300-Tout_rt2300); %W

%RT3000
Tin_rt3000 = (rt3000T1+rt3000T2)/2; %K
Tout_rt3000 = (rt3000T3+rt3000T4)/2; %K
Tavg_rt3000 = (Tin_rt3000+Tout_rt3000)/2;
cp_rt3000 = 4184*(0.2269807*exp((0.000097247*(Tavg_rt3000*(9/5))))); %J/kg-K
q_rt3000 = m_dotRT3000.*cp_rt3000.*(Tin_rt3000-Tout_rt3000); %W

%MC800
Tin_mc800 = (mc800T1+mc800T2)/2; %K
Tout_mc800 = (mc800T3+mc800T4)/2; %K
Tavg_mc800 = (Tin_mc800+Tout_mc800)/2;
cp_mc800 = 4184*(0.2269807*exp((0.000097247*(Tavg_mc800*(9/5))))); %J/kg-K
q_mc800 = m_dotMC800.*cp_mc800.*(Tin_mc800-Tout_mc800); %W

%MC1200
Tin_mc1200 = (mc1200T1+mc1200T2)/2; %K
Tout_mc1200 = (mc1200T3+mc1200T4)/2; %K
Tavg_mc1200 = (Tin_mc1200+Tout_mc1200)/2;
cp_mc1200 = 4184*(0.2269807*exp((0.000097247*(Tavg_mc1200*(9/5))))); %J/kg-K
q_mc1200 = m_dotMC1200.*cp_mc1200.*(Tin_mc1200-Tout_mc1200); %W

%MC2300
Tin_mc2300 = (mc2300T1+mc2300T2)/2; %K
Tout_mc2300 = (mc2300T3+mc2300T4)/2; %K
Tavg_mc2300 = (Tin_mc2300+Tout_mc2300)/2;
cp_mc2300 = 4184*(0.2269807*exp((0.000097247*(Tavg_mc2300*(9/5))))); %J/kg-K
q_mc2300 = m_dotMC2300.*cp_mc2300.*(Tin_mc2300-Tout_mc2300); %W

%MC3000
Tin_mc3000 = (mc3000T1+mc3000T2)/2; %K
Tout_mc3000 = (mc3000T3+mc3000T4)/2; %K
Tavg_mc3000 = (Tin_mc3000+Tout_mc3000)/2;
cp_mc3000 = 4184*(0.2269807*exp((0.000097247*(Tavg_mc3000*(9/5))))); %J/kg-K
q_mc3000 = m_dotMC3000.*cp_mc3000.*(Tin_mc3000-Tout_mc3000); %W

%PA800
```

```
Tin_pa800 = (pa800T1+pa800T2)/2; %K
Tout_pa800 = (pa800T3+pa800T4)/2; %K
Tavg_pa800 = (Tin_pa800+Tout_pa800)/2;
cp_pa800 = 4184*(0.2269807*exp((0.000097247*(Tavg_pa800*(9/5))))); %J/kg-K
q_pa800 = m_dotPA800.*cp_pa800.*(Tin_pa800-Tout_pa800); %W

%PA1200
Tin_pa1200 = (pa1200T1+pa1200T2)/2; %K
Tout_pa1200 = (pa1200T3+pa1200T4)/2; %K
Tavg_pa1200 = (Tin_pa1200+Tout_pa1200)/2;
cp_pa1200 = 4184*(0.2269807*exp((0.000097247*(Tavg_pa1200*(9/5))))); %J/kg-K
q_pa1200 = m_dotPA1200.*cp_pa1200.*(Tin_pa1200-Tout_pa1200); %W

%PA2300
Tin_pa2300 = (pa2300T1+pa2300T2)/2; %K
Tout_pa2300 = (pa2300T3+pa2300T4)/2; %K
Tavg_pa2300 = (Tin_pa2300+Tout_pa2300)/2;
cp_pa2300 = 4184*(0.2269807*exp((0.000097247*(Tavg_pa2300*(9/5))))); %J/kg-K
q_pa2300 = m_dotPA2300.*cp_pa2300.*(Tin_pa2300-Tout_pa2300); %W

%PA3000
Tin_pa3000 = (pa3000T1+pa3000T2)/2; %K
Tout_pa3000 = (pa3000T3+pa3000T4)/2; %K
Tavg_pa3000 = (Tin_pa3000+Tout_pa3000)/2;
cp_pa3000 = 4184*(0.2269807*exp((0.000097247*(Tavg_pa3000*(9/5))))); %J/kg-K
q_pa3000 = m_dotPA3000.*cp_pa3000.*(Tin_pa3000-Tout_pa3000); %W

%Method 2 - Find the average heat transfer taken over the entire transient

%RT800
m2_Tin_rt800 = mean((rt800T1+rt800T2)/2); %K
m2_Tout_rt800 = mean((rt800T3+rt800T4)/2); %K
m2_Tavg_rt800 = (m2_Tin_rt800+m2_Tout_rt800)/2;
m2_cp_rt800 = 4184*(0.2269807*exp((0.000097247*(m2_Tavg_rt800*(9/5)))));
%J/kg-K
m2_q_rt800 = m_dotRT800.*m2_cp_rt800.*(m2_Tin_rt800-m2_Tout_rt800); %W
m2_q_rt800_array = zeros(length(rt800time),1);
m2_q_rt800_array(:,1) = m2_q_rt800;

%RT1200
m2_Tin_rt1200 = mean((rt1200T1+rt1200T2)/2); %K
m2_Tout_rt1200 = mean((rt1200T3+rt1200T4)/2); %K
m2_Tavg_rt1200 = (m2_Tin_rt1200+m2_Tout_rt1200)/2;
m2_cp_rt1200 = 4184*(0.2269807*exp((0.000097247*(m2_Tavg_rt1200*(9/5)))));
%J/kg-K
m2_q_rt1200 = m_dotRT1200.*m2_cp_rt1200.*(m2_Tin_rt1200-m2_Tout_rt1200); %W
m2_q_rt1200_array = zeros(length(rt1200time),1);
m2_q_rt1200_array(:,1) = m2_q_rt1200;

%RT2300
m2_Tin_rt2300 = mean((rt2300T1+rt2300T2)/2); %K
m2_Tout_rt2300 = mean((rt2300T3+rt2300T4)/2); %K
m2_Tavg_rt2300 = (m2_Tin_rt2300+m2_Tout_rt2300)/2;
m2_cp_rt2300 = 4184*(0.2269807*exp((0.000097247*(m2_Tavg_rt2300*(9/5)))));
%J/kg-K
```

```
m2_q_rt2300 = m_dotRT2300.*m2_cp_rt2300.*(m2_Tin_rt2300-m2_Tout_rt2300); %W
m2_q_rt2300_array = zeros(length(rt2300time),1);
m2_q_rt2300_array(:,1) = m2_q_rt2300;

%RT3000
m2_Tin_rt3000 = mean((rt3000T1+rt3000T2)/2); %K
m2_Tout_rt3000 = mean((rt3000T3+rt3000T4)/2); %K
m2_Tavg_rt3000 = (m2_Tin_rt3000+m2_Tout_rt3000)/2;
m2_cp_rt3000 = 4184*(0.2269807*exp((0.000097247*(m2_Tavg_rt3000*(9/5)))));
%J/kg-K
m2_q_rt3000 = m_dotRT3000.*m2_cp_rt3000.*(m2_Tin_rt3000-m2_Tout_rt3000); %W
m2_q_rt3000_array = zeros(length(rt3000time),1);
m2_q_rt3000_array(:,1) = m2_q_rt3000;

%MC800
m2_Tin_mc800 = mean((mc800T1+mc800T2)/2); %K
m2_Tout_mc800 = mean((mc800T3+mc800T4)/2); %K
m2_Tavg_mc800 = (m2_Tin_mc800+m2_Tout_mc800)/2;
m2_cp_mc800 = 4184*(0.2269807*exp((0.000097247*(m2_Tavg_mc800*(9/5)))));
%J/kg-K
m2_q_mc800 = m_dotMC800.*m2_cp_mc800.*(m2_Tin_mc800-m2_Tout_mc800); %W
m2_q_mc800_array = zeros(length(mc800time),1);
m2_q_mc800_array(:,1) = m2_q_mc800;

%MC1200
m2_Tin_mc1200 = mean((mc1200T1+mc1200T2)/2); %K
m2_Tout_mc1200 = mean((mc1200T3+mc1200T4)/2); %K
m2_Tavg_mc1200 = (m2_Tin_mc1200+m2_Tout_mc1200)/2;
m2_cp_mc1200 = 4184*(0.2269807*exp((0.000097247*(m2_Tavg_mc1200*(9/5)))));
%J/kg-K
m2_q_mc1200 = m_dotMC1200.*m2_cp_mc1200.*(m2_Tin_mc1200-m2_Tout_mc1200); %W
m2_q_mc1200_array = zeros(length(mc1200time),1);
m2_q_mc1200_array(:,1) = m2_q_mc1200;

%MC2300
m2_Tin_mc2300 = mean((mc2300T1+mc2300T2)/2); %K
m2_Tout_mc2300 = mean((mc2300T3+mc2300T4)/2); %K
m2_Tavg_mc2300 = (m2_Tin_mc2300+m2_Tout_mc2300)/2;
m2_cp_mc2300 = 4184*(0.2269807*exp((0.000097247*(m2_Tavg_mc2300*(9/5)))));
%J/kg-K
m2_q_mc2300 = m_dotMC2300.*m2_cp_mc2300.*(m2_Tin_mc2300-m2_Tout_mc2300); %W
m2_q_mc2300_array = zeros(length(mc2300time),1);
m2_q_mc2300_array(:,1) = m2_q_mc2300;

%MC3000
m2_Tin_mc3000 = mean((mc3000T1+mc3000T2)/2); %K
m2_Tout_mc3000 = mean((mc3000T3+mc3000T4)/2); %K
m2_Tavg_mc3000 = (m2_Tin_mc3000+m2_Tout_mc3000)/2;
m2_cp_mc3000 = 4184*(0.2269807*exp((0.000097247*(m2_Tavg_mc3000*(9/5)))));
%J/kg-K
m2_q_mc3000 = m_dotMC3000.*m2_cp_mc3000.*(m2_Tin_mc3000-m2_Tout_mc3000); %W
m2_q_mc3000_array = zeros(length(mc3000time),1);
m2_q_mc3000_array(:,1) = m2_q_mc3000;

%PA800
m2_Tin_pa800 = mean((pa800T1+pa800T2)/2); %K
```

```
m2_Tout_pa800 = mean((pa800T3+pa800T4)/2); %K
m2_Tavg_pa800 = (m2_Tin_pa800+m2_Tout_pa800)/2;
m2_cp_pa800 = 4184*(0.2269807*exp((0.000097247*(m2_Tavg_pa800*(9/5))))); 
%J/kg-K
m2_q_pa800 = m_dotPA800.*m2_cp_pa800.*(m2_Tin_pa800-m2_Tout_pa800); %W
m2_q_pa800_array = zeros(length(pa800time),1);
m2_q_pa800_array(:,1) = m2_q_pa800;

%PA1200
m2_Tin_pa1200 = mean((pa1200T1+pa1200T2)/2); %K
m2_Tout_pa1200 = mean((pa1200T3+pa1200T4)/2); %K
m2_Tavg_pa1200 = (m2_Tin_pa1200+m2_Tout_pa1200)/2;
m2_cp_pa1200 = 4184*(0.2269807*exp((0.000097247*(m2_Tavg_pa1200*(9/5))))); 
%J/kg-K
m2_q_pa1200 = m_dotPA1200.*m2_cp_pa1200.*(m2_Tin_pa1200-m2_Tout_pa1200); %W
m2_q_pa1200_array = zeros(length(pa1200time),1);
m2_q_pa1200_array(:,1) = m2_q_pa1200;

%PA2300
m2_Tin_pa2300 = mean((pa2300T1+pa2300T2)/2); %K
m2_Tout_pa2300 = mean((pa2300T3+pa2300T4)/2); %K
m2_Tavg_pa2300 = (m2_Tin_pa2300+m2_Tout_pa2300)/2;
m2_cp_pa2300 = 4184*(0.2269807*exp((0.000097247*(m2_Tavg_pa2300*(9/5))))); 
%J/kg-K
m2_q_pa2300 = m_dotPA2300.*m2_cp_pa2300.*(m2_Tin_pa2300-m2_Tout_pa2300); %W
m2_q_pa2300_array = zeros(length(pa2300time),1);
m2_q_pa2300_array(:,1) = m2_q_pa2300;

%PA3000
m2_Tin_pa3000 = mean((pa3000T1+pa3000T2)/2); %K
m2_Tout_pa3000 = mean((pa3000T3+pa3000T4)/2); %K
m2_Tavg_pa3000 = (m2_Tin_pa3000+m2_Tout_pa3000)/2;
m2_cp_pa3000 = 4184*(0.2269807*exp((0.000097247*(m2_Tavg_pa3000*(9/5))))); 
%J/kg-K
m2_q_pa3000 = m_dotPA3000.*m2_cp_pa3000.*(m2_Tin_pa3000-m2_Tout_pa3000); %W
m2_q_pa3000_array = zeros(length(pa3000time),1);
m2_q_pa3000_array(:,1) = m2_q_pa3000;

%Generate figures

%Pin Array
figure()
plot(pa800time,q_pa800,'-k',pa800time,m2_q_pa800_array,'-
.k',pa1200time,q_pa1200,'-r',pa1200time,m2_q_pa1200_array,'-
.r',pa2300time,q_pa2300,'-b',pa2300time,m2_q_pa2300_array,'-
.b',pa3000time,q_pa3000,'-m',pa3000time,m2_q_pa3000_array,'-.m')
title('Pin Array Heat Transfer Rate')
xlabel('Time (s)')
ylabel('q(t) [W]')
legend('Re = 800','Re = 800 Avg','Re = 1200','Re = 1200 Avg','Re = 2300','Re
= 2300 Avg','Re = 3000','Re = 3000 Avg','Location','northwest')

%Microchannel
figure()
plot(mc800time,q_mc800,'-k',mc800time,m2_q_mc800_array,'-
.k',mc1200time,q_mc1200,'-r',mc1200time,m2_q_mc1200_array,'-
```

```
.r',mc2300time,q_mc2300,'-b',mc2300time,m2_q_mc2300_array,'-
.b',mc3000time,q_mc3000,'-m',mc3000time,m2_q_mc3000_array,'-.m')
title('Microchannel Heat Transfer Rate')
xlabel('Time (s)')
ylabel('q(t) [W]')
legend('Re = 800','Re = 800 Avg','Re = 1200','Re = 1200 Avg','Re = 2300','Re
= 2300 Avg','Re = 3000','Re = 3000 Avg','Location','northwest')

%Ribbed Turbulator
figure()
plot(rt800time,q_rt800,'-k',rt800time,m2_q_rt800_array,'-
.k',rt1200time,q_rt1200,'-r',rt1200time,m2_q_rt1200_array,'-
.r',rt2300time,q_rt2300,'-b',rt2300time,m2_q_rt2300_array,'-
.b',rt3000time,q_rt3000,'-m',rt3000time,m2_q_rt3000_array,'-.m')
title('Ribbed Turbulator Heat Transfer Rate')
xlabel('Time (s)')
ylabel('q(t) [W]')
legend('Re = 800','Re = 800 Avg','Re = 1200','Re = 1200 Avg','Re = 2300','Re
= 2300 Avg','Re = 3000','Re = 3000 Avg','Location','northwest')

%Re = 800
figure()
plot(rt800time,q_rt800,'-k',rt800time,m2_q_rt800_array,'-
.k',pa800time,q_pa800,'-r',pa800time,m2_q_pa800_array,'-
.r',mc800time,q_mc800,'-b',mc800time,m2_q_mc800_array,'-.b')
title('Heat Transfer Rate at Re = 800')
xlabel('Time (s)')
ylabel('q(t) [W]')
%legend('Ribbed Turbulator','Ribbed Turbulator Avg','Pin Array','Pin Array
Avg','Microchannels','Microchannel Avg','Location','southeast')

%Re = 1200
figure()
plot(rt1200time,q_rt1200,'-k',rt1200time,m2_q_rt1200_array,'-
.k',pa1200time,q_pa1200,'-r',pa1200time,m2_q_pa1200_array,'-
.r',mc1200time,q_mc1200,'-b',mc1200time,m2_q_mc1200_array,'-.b')
title('Heat Transfer Rate at Re = 1200')
xlabel('Time (s)')
ylabel('q(t) [W]')
%legend('Ribbed Turbulator','Ribbed Turbulator Avg','Pin Array','Pin Array
Avg','Microchannels','Microchannel Avg','Location','southeast')

%Re = 2300
figure()
plot(rt2300time,q_rt2300,'-k',rt2300time,m2_q_rt2300_array,'-
.k',pa2300time,q_pa2300,'-r',pa2300time,m2_q_pa2300_array,'-
.r',mc2300time,q_mc2300,'-b',mc2300time,m2_q_mc2300_array,'-.b')
title('Heat Transfer Rate at Re = 2300')
xlabel('Time (s)')
ylabel('q(t) [W]')
%legend('Ribbed Turbulator','Ribbed Turbulator Avg','Pin Array','Pin Array
Avg','Microchannels','Microchannel Avg','Location','southeast')

%Re = 3000
figure()
```

```
plot(rt3000time,q_rt3000,'-k',rt3000time,m2_q_rt3000_array,'-
.k',pa3000time,q_pa3000,'-r',pa3000time,m2_q_pa3000_array,'-
.r',mc3000time,q_mc3000,'-b',mc3000time,m2_q_mc3000_array,'-.b')
title('Heat Transfer Rate at Re = 3000')
xlabel('Time (s)')
ylabel('q(t) [W]')
%legend('Ribbed Turbulator','Ribbed Turbulator Avg','Pin Array','Pin Array
Avg','Microchannels','Microchannel Avg','Location','southeast')


%cp = 4184*(0.2269807*exp((0.000097247*(T*(9/5)))) %J/kg-K
```

A3: IR Temperature Profile Transformation for FEM Model Surface Boundary

```
%Transformation Code
%%
clc; clear all; close all;
%Extract Test Piece Data from Raw Data
clear; clc; close all;
%Import raw data from csv file
fileName = 'Test1_900.csv';
rawData = csvread(fileName);
%Create contour of raw data for point selection
contourf(rawData,25);
axis equal;
%Select two points on test piece to bound matrix containing
%only the test article
%   Two points selected to make square matrix
%   First point should be upper left point
%   Second point should be lower right point
%       xp = streamwise points
%       yp = spanwise points
[xp,yp] = ginput(2);
%Round x & y to whole numbers to match pixel distribution of
%the raw data
xp = round(xp);
yp = round(yp);
%Generate sub matrix containing the test piece pizels from
%the selected boundaries points
subM = rawData(yp(2):yp(1),xp(1):xp(2));
subMfixed = flipud(subM);
%Second Time Point
fileName1 = 'Test1_300.csv';
rawData1 = csvread(fileName1);
%Generate sub matrix containing the test piece pizels from
%the selected boundaries points
subM1 = rawData1(yp(2):yp(1),xp(1):xp(2));
subM1fixed = flipud(subM1);

%Determine the Size of the chosen condensed image of the part
[yPos,xPos] = size(subM1fixed);
%Establish the pertinent length and height dimensions of the part
xLength = 0.0444500; %[m]
yLength = 0.06372219; %[m]
%Set the Starting Position of every point within the image
xStart = 0.5*(xLength/xPos);
%yStart = yLength - 0.5*(yLength/yPos);
yStart = 0.5*(yLength/yPos);
%Find the distance between center points of an element
xDist = xLength/xPos;
yDist = yLength/yPos;
%Generate the pixel grid x & y values for every poin on the grid
a = 1:1:xPos;
%Calculate each x pixel value and store as an array
xPixelValue = xStart + (a-1).*xDist;
b = 1:1:yPos;
%Calculate each y pixel value and store as an array
```

```
yPixelValue = yStart + (b-1).*yDist;

% subM(:,:) =  M(yi(2):yi(1),xi(1):xi(2));
% %Plot Contour
% figure
% h = contourf(subM,75,'linecolor','none');
% colormap('jet')
% axis equal;
% colorbar('southoutside')
% colorbar.Label.String = 'Surface Temperature (F)';
% xlabel('Streamwise Direction')
% ylabel('Spanwise Direction')
% title('Temperature Profile - Microchannel')

% tempDistOutputCSV = cell(xPos*yPos+1,5);
tempDistOutputLabel = ['X','Y','Z','T','s','h'];

%Guess for h
h = 35; %[W/m^2-K]

%Iterate through files in the data directory

    %Find the time step of the file
    if numel(fileName)==11
        time = str2num(fileName(end-4:end-3));
    elseif numel(fileName)==12
        time = str2num(fileName(end-5:end-3));
    elseif numel(fileName)==13
        time = str2num(fileName(end-6:end-3));
    elseif numel(fileName)==14
        time = str2num(fileName(end-7:end-3));
    end
    %Designate a file name to write to containing the correct time step
    writeFile = sprintf('%s_%d.csv','adjTemperatureDist',time);
    dlmwrite(writeFile,tempDistOutputLabel,'delimiter',',');

    %Convert Temperatures from fahrenheit to celsius
    subMfixed = (subMfixed-32)*(5/9)+273.15;

    %Because the model surface is in the (Y,Z) plane, set all x values equal
to
    %zero
    xModel = 0;
    %Set Counter for file row assignments
    count = 1;
    %tempDistOutputCSV(1,) = ['X','Y','Z','Temp','Time'];
    for x = 1:1:xPos
        for y=1:1:yPos
            %Place appropriate temperature into the output file for this
            %position
            %Within the model: the y data corresponds to y data on the image,
            %the z axis corresponds to the x data from the image, and the x
            %axis corresponds to the z axis of the image
            tempDistOutputCSV(count,4) = subMfixed(y,x);
            %Input appropriate Z value into output csv for used on the model
```

```
            tempDistOutputCSV(count,1) = xModel;
            tempDistOutputCSV(count,2) = yPixelValue(y);
            tempDistOutputCSV(count,3) = xPixelValue(x);
            tempDistOutputCSV(count,5) = time/30;
            tempDistOutputCSV(count,6) = h;
            count = count+1;
        end
    end
%Designate a file name to write to containing the correct time step
dlmwrite(writeFile,tempDistOutputCSV,'delimiter',',','-append');
```

A4: Nusselt Number Evaluation

```
%Heat Transfer Calculations
%% Measured or Calculated Values Values
close all;
k = 0.3; %W/m-K
%   Mass Flow
m_dot_pin = [24.0, 36.1, 69.1]; %SLPM
m_dot_mc = [15.1, 22.7, 43.5,56.8]; %SLPM
m_dot_rib = [23.9, 35.9, 68.8]; %SLPM
%   Reynolds Number
Re = [800, 1200, 2300, 3000];
Re_pa = [800, 1200, 2300];
%   HTC
htc_pa = [8.237, 37.234, 62.196];
htc_mc = [2.150, 3.658, 5.378,8.209];
htc_rt = [4.691, 10.850, 23.940];
%   Hydraulic Diameter of Cooling Feature
Dh_pa = [0.004, 0.004, 0.004]; %m
Dh_mc = [0.0005, 0.0005, 0.0005, 0.0005]; %m
Dh_rt = [0.0067, 0.0067, 0.0067]; %m
%   Cross Sectional Area of Channel
Acs_pa = 2.769e-04;
Acs_mc = (2.8125e-07)*35;
Acs_rt = 2.087e-04;%   Normalized ratio of Feature Characteristic Length to
Channel
%   Characteristic Length normalized by ratio of feature length to Channel
%   cross sectional area
Aratio_pa = Acs_pa./Acs_pa;
Aratio_mc = Acs_pa./Acs_mc;
Aratio_rt = Acs_pa./Acs_rt;
%   Nusselt Number based on Cooling Feature Hydraulic Diameter
Nu_pa_Dh_feature = htc_pa.*Dh_pa./k;
Nu_mc_Dh_feature = htc_mc.*Dh_mc./k;
Nu_rt_Dh_feature = htc_rt.*Dh_rt./k;
%   Nusselt Number based on Total Channel Cross Sectional Area
Nu_pa_csChannel = htc_pa.*Acs_pa./k;
Nu_mc_csChannel = htc_mc.*Acs_mc./k;
Nu_rt_csChannel = htc_rt.*Acs_rt./k;
%   Nusselt Number Adjusted by Characteristic Area Ratio wrt Feature Dh
Nu_Aratio_Dh_pa = Nu_pa_Dh_feature.*Aratio_pa;
Nu_Aratio_Dh_mc = Nu_mc_Dh_feature.*Aratio_mc;
Nu_Aratio_Dh_rt = Nu_rt_Dh_feature.*Aratio_rt;
%   Nusselt Number Adjusted by Characteristic Area Ratio wrt Channel
%   Characteristic Length
Nu_Aratio_csA_pa = Nu_pa_csChannel.*Aratio_pa;
Nu_Aratio_csA_mc = Nu_mc_csChannel.*Aratio_mc;
Nu_Aratio_csA_rt = Nu_rt_csChannel.*Aratio_rt;

%% Plots

%Nusselt Number with Respect to Feature Hydraulic Diameter

    %Vs. Mass Flow Rate (SLPM)
    figure()
```

```
    plot(m_dot_pin,Nu_pa_Dh_feature,'-or',m_dot_mc,Nu_mc_Dh_feature,'-
ob',m_dot_rib,Nu_rt_Dh_feature,'-ok')
    xlabel('Mass Flow Rate (SLPM)')
    ylabel('Nu_{avg}')
    legend('Pin Array','Microchannels','Ribbed Turbulators')
    title('Surface Average Nusselt Number w.r.t Feature Hydraulic Diameter')
    %Vs. Reynolds Number
    figure()
    plot(Re_pa,Nu_pa_Dh_feature,'-or',Re,Nu_mc_Dh_feature,'-
ob',Re_pa,Nu_rt_Dh_feature,'-ok')
    xlabel('Re')
    ylabel('Nu_{avg}')
    legend('Pin Array','Microchannels','Ribbed Turbulators')
    title('Surface Average Nusselt Number w.r.t Feature Hydraulic Diameter')

%Nusselt Number Adjusted by Characteristic Area Ratio wrt Feature Dh

    %Vs. Mass Flow Rate (SLPM)
    figure()
    plot(m_dot_pin,Nu_Aratio_Dh_pa,'-or',m_dot_mc,Nu_Aratio_Dh_mc,'-
ob',m_dot_rib,Nu_Aratio_Dh_rt,'-ok')
    xlabel('Mass Flow Rate (SLPM)')
    ylabel('Nu_{avg}(A_feature/A_cs)')
    legend('Pin Array','Microchannels','Ribbed Turbulators')
    title('Area Adjusted Surface Average Nusselt Number w.r.t Feature
Hydraulic Diameter')
    %Vs. Reynolds Number
    figure()
    plot(Re_pa,Nu_Aratio_Dh_pa,'-or',Re,Nu_Aratio_Dh_mc,'-
ob',Re_pa,Nu_Aratio_Dh_rt,'-ok')
    xlabel('Re')
    ylabel('Nu_{avg}(A_feature/A_cs)')
    legend('Pin Array','Microchannels','Ribbed Turbulators')
    title('Area Adjusted Surface Average Nusselt Number w.r.t Feature
Hydraulic Diameter')
```